SOFIA UNIVERSITY
ST. KLIMENT OHRIDSKI

Investigation of the fine and hyperfine structure of the $c^3\Sigma^+$ state in KRb

Autoreferat written in the
Sofia University St. Kliment Ohridski
under the supervision of prof. Asen Pashov.

Velizar Rosenov Stoyanov

May 21, 2024

Acknowledgements

Abstract

The hyperfine structure of the transitions in the $(X, v'' = 0 \to (B, c), v' = 2)$ band system in $^{39}\text{K}^{85}\text{Rb}$ and $^{39}\text{K}^{87}\text{Rb}$ is studied by using several selective Doppler-free spectroscopy techniques. Significant splitting of the line profiles is observable for the $B^1\Pi$ state levels coupled to the $c^3\Sigma^+$ levels through spin-orbit interactions. The splitting is the result from an interplay between spin-spin, spin-rotation, spin-orbit interactions and the Fermi-contact interaction between the electron's spin and the nuclear spins. Energy shifts of the perturbed levels were analyzed and modeled within the effective Hamiltonian approach. Molecular and coupling constants were determined, which successfully model the experimental observations. Although the highest experimental resolution of 50 MHz was not sufficient to resolve entirely the hyperfine structure, the model successfully explains the line broadening in $^{39}\text{K}^{85}\text{Rb}$ and the line splitting in $^{39}\text{K}^{87}\text{Rb}$.

Contents

Chapter 1

Introduction

Ever since the invention of the laser, molecular spectroscopy has gone through a renaissance. The accuracy and resolving power of the measurements were greatly increased and the different spectroscopic techniques that have been invented gave opportunity of studying the molecular structures far more precisely than before. Among other, the diatomic alkali-metal molecules have been, and still are, the subject of many different experimental and theoretical investigations. They are attractive for experimentalists because they are relatively easy to produce and their rich optical spectrum can be covered with various types of available laser sources. The homonuclear alkali diatomics (Li_2, Na_2, K_2, Rb_2 and Cs_2) are among the experimentally best studied diatomic molecules and they have often served as testing ground for new spectroscopic techniques. On the other hand many different kinds of theoretical calculations are devoted to the lighter alkali-metal diatomics because of their relatively simple electronic structure - two valence electrons outside closed shells.

Of all the different homo and heteronuclear alkali diatomic molecules the KRb is of particular interest, because the atomic levels $K(4p^2P_j)$ are in close proximity to the atomic levels $Rb(5p^2P_j)$: the energies of the $K(4p^2P_{3/2})$, $K(4p^2P_{1/2})$, $Rb(5p^2P_{3/2})$ and $Rb(5p^2P_{1/2})$ levels are, respectively, 13042.89, 12985.17, 12816.56 and 12578.96 cm^{-1}[1]. Thus a strong coupling between the excited electronic states correlated to these asymptotes is expected. Wang and Stwalley [2] predicted that KRb has considerably stronger excited long-range interactions than any other heteronuclear alkali diatomic molecule and has very favorable Franck-Condon factors for photoassociation [3, 4]. Another advantage of the KRb molecule is that, as a heteronuclear molecule, it possesses permanent dipole moment giving the possibility of external filed control. Photoassociative production and trapping of ultracold KRb molecules (not in their ground $X^1\Sigma^+$, $v'' = 0$, $J'' = 0$ state) was demonstrated [5, 6]. Ultracold Feshbach molecules and Feshbach resonances were also formed and observed by magnetoassociation [7–9]. A lot of efforts have then been made for production of ultracold molecules in their ground state and one way of achieving

this is by Stimulated Raman adiabatic passage (STIRAP) [10]. Ni et al. [11] have successfully transferred weakly bound magnetoassociated ^{40}K^{87}Rb molecules into their ground state using STIRAP. Just two years after them this was also done with photoassociated molecules as well [12, 13].

From experimental point of view, Walter and Barratt [14] are the first to show the existence of heteronuclear alkali compound in vapor state by measuring their absorption spectra. For KRb they observed a structureless band with a maximum at 459.9 nm. Prior to any other spectroscopic studies, sensitized fluorescence in rubidium vapor, induced by collision with excited potassium atoms was investigated to determine the total cross sections for inelastic collisions between excited potassium atoms and rubidium atoms in their ground states [15–18]. Beuc et al. observed diffuse bands at 597, 586.7 and 569 nm [19] and additional satellite bands were observed by Skenderović et al. [20].

The ground state $X^1\Sigma^+$ was first experimentally characterized at high resolution by Ross et al. [21]. The KRb molecules were produced in heat pipe and excited using a Ti:sapphire laser. The subsequent $A(2)^1\Sigma^+ - X^1\Sigma^+$ fluorescence spectra was recorded on a Fourier transform spectrometer (see figure 2.1 with the potential energy curves). With similar experimental setup, though at better resolution, Amiot and Vergés [22] have substantially extended the experimental data and altogether with the lines from [21], have derived a potential energy curve for the ground state up to quite large internuclear distance of 10.419 Å. But the most accurate, up to date, $X^1\Sigma^+$ state potential energy curve (up to 14.8 Å) is derived by Pashov and co-workers [23], through a coupled channels fitting routine. They have used the perturbations in the $B(1)^1\Pi$ state by the closely lying $c(2)^3\Sigma^+$ and $b(1)^3\Pi$ triplet states as a window to record fluorescence with a Fourier-transform spectrometer down to both $X^1\Sigma^+$ and $a^3\Sigma^+$ states. Thus they have extended the experimental data from [22] even more and make use also of the Feshbach resonance positions from [7]. From the fit the $a^3\Sigma^+$ state potential is derived as well. In another study, again with Fourier-transform spectroscopy the spin-orbit coupled $A(2)^1\Sigma^+$ and $b(1)^3\Pi$ states were studied and deperturbation analysis of the data yield potential energy curves for both excited electronic states [24].

By using optical-optical double resonance polarization spectroscopy Okada et al. [25] and Kasahara et al.[26] were the first to have studied the excited $B(1)^1\Pi$ and $2^1\Pi$ electronic states. The $2^1\Pi$ state was studied also in [27], by recording the fluorescence in the $3^1\Pi - 2^1\Pi$ system, after excitation with fixed Ar$^+$ laser frequencies. These reports have shown occurrence of many perturbations, some of them used in [23] as already mentioned. The $3^1\Sigma^+$ state energy levels up to $v = 15$ and those of the $c(2)^3\Sigma^+$ state up to $v = 14$ were also by recording the fluorescence from the $3^1\Pi$ state [28, 29].

Lee et al. have prepared KRb molecules in their natural isotopic composition in a pulsed molecular beam. Using resonance enhanced two photon ionization

the group has observed and identified electric quadrupole and spin-forbidden transitions in the $1^1\Delta - X^1\Sigma^+$ and $3^3\Sigma^+ - X^1\Sigma^+$ band systems, respectively [30, 31]. In [31] the hyperfine structure of the $3^3\Sigma^+$ state was found to be mainly dominated by the Fermi-contact interaction between the Rb nuclear spin and the unpaired electronic spins. With the same experimental apparatus more band systems around 480 nm [32] and 420 nm [33] were recorded and even higher excited $1^3\Delta_1, 4^1\Sigma^+, 5^1\Sigma^+$ and $4^1\Pi, 7^1\Sigma, 5^1\Pi$ states were identified.

The establishment of cold KRb photoassociated molecules gave the opportunity for investigating excited electronic states by starting from high vibrational $X^1\Sigma^+$ or $a^3\Sigma^+$ levels. The molecular wave function of such levels is non-zero mainly at large internuclear distances, therefore having favorable Franck-Condon factors with excited terms that are not accessible from the deeply bound $X^1\Sigma^+$ levels. In this way photoassociation spectroscopy is somewhat complementary to the experiments in heat pipe or molecular beam. With the high resolution spectra from photoassociation spectroscopy the first few rotational terms for some high vibrational levels of the excited electronic states correlated with the $K(4s^2 S_{1/2})+Rb(5p^2 P_{1/2,3/2})$ asymptotes were examined [6]. These spectra were recorded by tuning a continuous wave laser that excites free-bound transitions, whereafter fluorescence to the $a^3\Sigma^+$ state a second strong pulsed laser ionizes the molecules by two photon excitation. Similarly, but by fixing the frequency of the first laser and changing that of the second one, inevitably resulting in lower resolving power, Kim et al. [34] studied the band structure of the $2^3\Pi, 3^3\Sigma^+$ and $4^3\Sigma^+$ states. In another paper [35] the same group have studied the band structure to the coupled $B(1)^1\Pi, c(2)^3\Sigma^+$ and $b(1)^3\Pi$ states using both ultracold molecules and molecular beam experiments. With such an experimental combination they gave prescription for optimal stimulated Raman transfer of ultacold molecules to their absolute ground state [36]. Also in searching for optimal path, by using photoassociated molecules and depletion spectroscopy, Aikawa et al. [37] have obtained high resolution rotational spectra for the first few rotational terms of the $3^1\Sigma^+(v' = 41 - 50)$ state, thus increasing what was know at that time from [28] for $v \le 15$. As in [34], Banerjee et al. [38] have also studied the $3^3\Sigma^+$ state up to the last $v' = 13$ level and observed broadening of the last band line due to predissociation. Wang et al.[39] have determined the dissociation energy of the ground state to be 4217.822(3) cm^{-1}, using depletion spectroscopy.

From theoretical point of view, approximate ground state spectroscopic constants for heteronuclear alkali molecules were obtained long ago by Cavaliére et al. [40] by interpolation methods. The generalized reduced potential curve method was set up by Jenc and Brandt [41, 42] and by Bludsky et al. [43], who derived preliminary ground state potential curves for several guesses of the dissociation energy value. An improved calculation of the dissociation energy for the X state was given later by Stwalley [44]. Long range studies and calculation of dispersion coefficients have been reported by several authors [45–49]. Ab initio calculation

of the electronic states, calculation of permanent and transition dipole moments, lifetimes and other molecular properties were reported in [50–62]. The most recent ab initio calculations are given by Jasik et al. [63].

It was mentioned above, that in [23] the $B(1)^1\Pi - c(2)^3\Sigma^+$ complex was used to observe fluorescence to the $a^3\Sigma^+$ state, following excitation from $X^1\Sigma^+$. In this study it was reported that the appearance of the hyperfine structure of the (B, c) $\rightarrow a^3\Sigma^+$ transitions changes by tuning the laser across the $X^1\Sigma^+ \rightarrow (B, c)$ Doppler profile. The only plausible explanation was the hyperfine structure of the (B, c) levels. In [25] Okada et al. did not thoroughly analyze the fine structure of the B state and the coupling with the c state, in order to come up with molecular constants. Also, Kim et al. [34] in their study did not obtain rotational resolved spectra for the (B, c) levels. And so far, the hyperfine structure was analyzed only for the $3^3\Sigma^+$ state. The still missing understanding of the coupling between the B and the c states and the hyperfine structure of their levels was the main motivation to undertake the present study. To conduct the investigation the goals we set are:

1. Develop experimental setup, including lasers and schemes for Doppler free spectroscopy.

2. Produce KRb molecules in a heat pipe and obtain optimum working conditions for Doppler free measurements.

3. Record and analyse high resolution spectra. Assign quantum numbers to the observed lines.

4. Develop theoretical model (including numerical routines) for the fine and the hyperfine structure of the $B - c\,(v_B = 2)$ rotation levels.

Chapter 2

The diatomic molecule effective Hamiltonian

The purpose of chapters 3,4 and 5 in the thesis is to present in a systematic manner the theoretical model, used afterwards with a numerical calculation to give explanation of the experimentally obtained spectra. Here the main steps will be outlined and only the important results will be given. General treatment on the subject can also be found in [64–67].

The diatomic molecule is treated as a quantum-mechanical system composed out of $n+2$ charged particles - n electrons and 2 nuclei. Models such as harmonic or anharmonic oscillator, rigid or non-rigid rotor and symmetrical top are not able to explain fine or hyperfine structure effects, thus not suitable to describe the experimentally observed data in this study. Consider some laboratory frame of reference, where $\boldsymbol{r}_i = (x_i, y_i, z_i)$ with $i = 1, 2, \ldots, n$ and $\boldsymbol{R}_\alpha = (X_\alpha, Y_\alpha, Z_\alpha)$ with $\alpha = 1, 2$ - designate the radius vectors of the electrons and the nuclei, respectively. The Hamiltonian of the system, when no external field is present, is

$$
\begin{aligned}
H = &-\sum_{\alpha=1}^{2} \frac{\hbar^2}{2M_\alpha} \nabla_\alpha^2 - \sum_{i=1}^{n} \frac{\hbar^2}{2m} \nabla_i^2 + \frac{Z_1 Z_2 e^2}{4\pi\epsilon_0} \frac{1}{|\boldsymbol{R}_1 - \boldsymbol{R}_2|} + \frac{e^2}{4\pi\epsilon_0} \sum_{i<j}^{n} \frac{1}{|\boldsymbol{r}_i - \boldsymbol{r}_j|} \\
&- \frac{e^2}{4\pi\epsilon_0} \sum_{i,\alpha=1}^{n,2} \frac{Z_\alpha}{|\boldsymbol{r}_i - \boldsymbol{R}_k|} + H(\boldsymbol{s}_i) + H(\boldsymbol{I}_\alpha),
\end{aligned}
\tag{2.1}
$$

where ϵ_0 is the vacuum permittivity constant, $\hbar$ the reduced Plank's constant, m is the mass of the electron, M_1, M_2 and Z_1, Z_2 are the masses and the charges of the nuclei; $\boldsymbol{s}_i$ is the i-th electron spin angular momentum operator, while $\boldsymbol{I}_\alpha$ are those for the nuclei. Nabla is the vector differential operator, whose form in Cartesian coordinates is $\nabla = (\partial/\partial x, \partial/\partial y, \partial/\partial z)$. The first two sums represent the kinetic energy operators of the particles. The third, forth and the fifth terms are the electrostatic potential energies between the particles. Interaction terms due to the

existence of the electron spin are included in $H(\boldsymbol{s}_i)$, whilst these that emerge from consideration of the nuclear spin are included in $H(\boldsymbol{I}_\alpha)$. Their explicit forms are given in equations (4.47-4.50) of chapter 4 in the thesis. Analytical solution of the stationary Schrödinger equation with this Hamiltonian is unthinkable, even more a numerical method is impractical to apply at this stage. A sequence of transformations, assumptions and simplification are made before reaching the point of applying any numerical methods.

The overall idea is to separate the variables in (2.1) as much as possible and then consider only that part of the Hamiltonian responsible not for the electronic, nor for the vibrational but for the rotational structure, by means of the spherical tensor algebra. To accomplish this a change of basis, going from the laboratory frame to the center of mass of the nuclei (not of the molecule) is made initially. Then another change is made to the so called molecular frame rotating with the nuclei. The Hamiltonian thus obtained would allow separation of the variables, where the motion of the electrons will depend only on the internuclear distance, but not on the rotation of the nuclei. The end result, where the Hamiltonian is separated into two parts is given by equations (3.49) and (3.88) in the thesis:

$$H_{\mathrm{ev}} = -\frac{\hbar^2}{2\mu R^2}\frac{\partial}{\partial R}R^2\frac{\partial}{\partial R} - \frac{\hbar^2}{2m}\sum_{i=1}^{n}\nabla_{r_i}^2 - \frac{\hbar^2}{2M}\sum_{i,j=1}^{n}\nabla_{r_i}.\nabla_{r_j}$$
$$+ U(R, \boldsymbol{r}_1, \ldots, \boldsymbol{r}_n), \quad (2.2)$$

$$H_{\mathrm{ang}} = B(\boldsymbol{J} - \boldsymbol{P})^2 + H(\boldsymbol{s}_i) + H(\boldsymbol{I}_\alpha). \quad (2.3)$$

where the first part represents the electronic and vibrational motion, while the second represents the angular motion, with $B = \hbar^2/2\mu R^2$. R here is the internuclear distance and the electronic coordinates are now written with respect to the molecule-fixed frame, which rotates with the nuclei and whose axis is coincident with the internuclear one. $\boldsymbol{J}$ is the total angular momentum exclusive of nuclear spin and $\boldsymbol{P} = \boldsymbol{L} + \boldsymbol{S}$ is sum of the total electronic orbital and spin angular momenta in the molecular frame.

There are in general two approaches, at this point: the effective Hamiltonian or the coupled channels. Although the second one is more general and global, we think that for the particular task the effective Hamiltonian approach is more appropriate for two reasons: (1) the spin-orbit mixing is small compared to the vibrational spacing of both B and c states (see figure 2.1 for the potential energy curves), so it is expected that a small number of wave functions spanning the subspace for the effective Hamiltonian method should be enough. (2) Treatment of the hyperfine structure within a global coupled channels model will lead to matrices of very large dimensions and would require significant computer power, which is not justified for the present set of experimental observations.
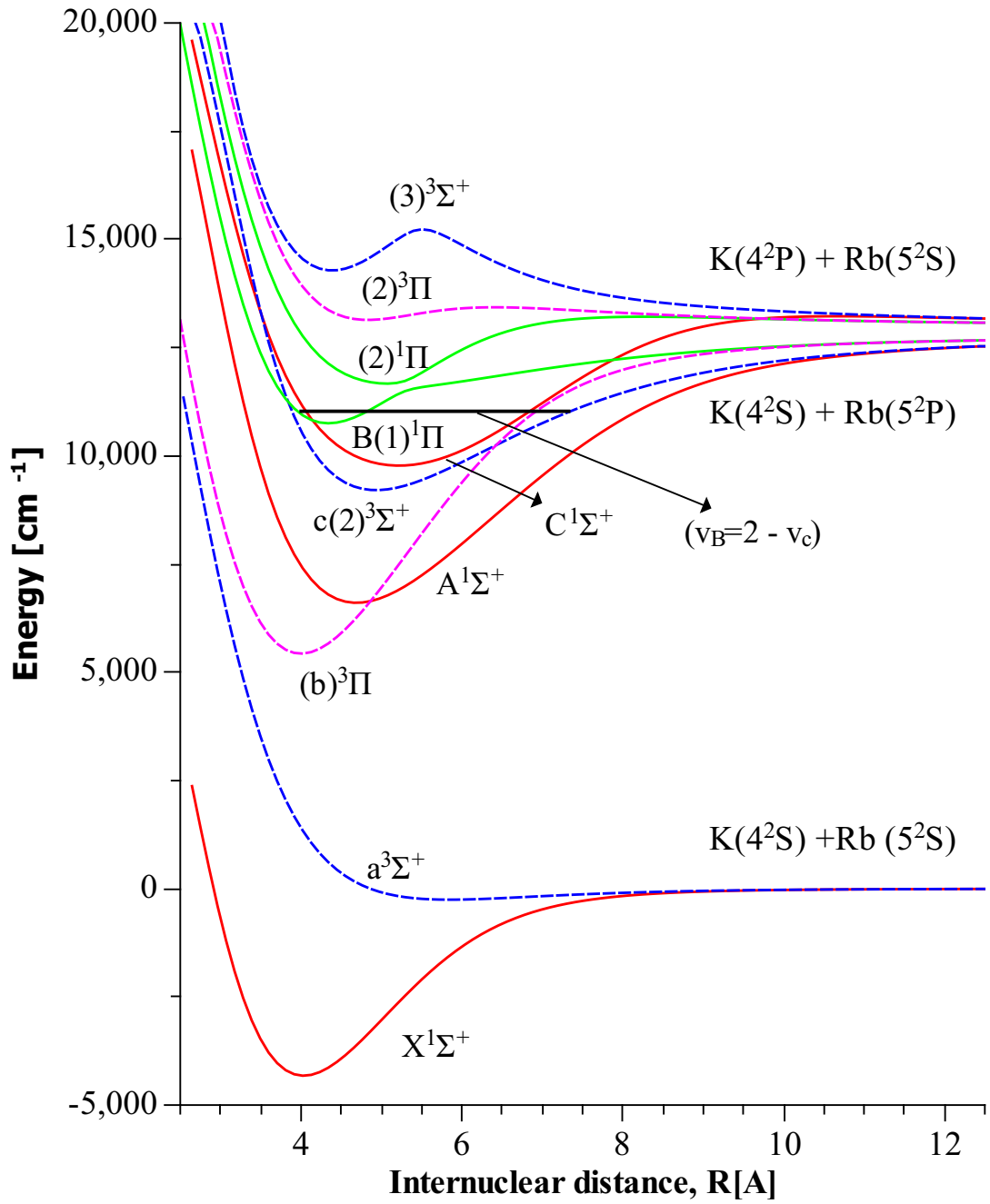
Figure 2.1: Theoretical adiabatic potential energy curves for selected KRb electronic states correlated to the lowest three dissociation limits, calculated in [63]. The upward arrow shows the transitions to the $(B^1\Pi, c^3\Sigma^+)$ complex excited by the laser. In the filtered laser excitation experiment the fluorescence to the $a^3\Sigma^+$ state $(c - a$ dashed arrow) is used.

The idea of the effective Hamiltonian method is instead of solving a system of coupled differential equations, to obtain a representation of the Hamiltonian in a subspace of functions, which is able to take into account the block off-diagonal matrix elements. This is very much alike the degenerate perturbation theory normally studied in quantum mechanics courses. This effective Hamiltonian can be obtained either by the Van Vleck contact transformation, or using projection operators. More information can be found in chapter 4 of the thesis. The vibronic part H_{ev} serves as zero-order approximation, while the angular part H_{ang} is treated as perturbation, which lifts up the degeneracy of the eigenstates in zero-order. The effective Hamiltonian in our case is restricted to act within a subspace of two vibronic levels. For the $B^1\Pi$ state the initial basis is given by equations (5.12, 5.13, thesis), which correspond to the symmetrized Hund's case (a_β-unequal) and for the $c^3\Sigma^+$ state by equations (5.38, 5.39, 5.40, thesis) corresponding to Hund's case ($b_{\beta J}$-unequal). As a result of the application of this perturbative approach, the operator form of the diatomic effective Hamiltonian is obtained (see equation 5.1, thesis)

$$
\begin{aligned}
H_{\text{eff}} = {}& H_{\text{ev}}^{(0)} + H_{\text{rot,eff}}^{(1)} + H_{\text{rot,eff}}^{(2)} + H_{\text{ss,eff}} + H_{\text{so,eff}} + H_{\text{sr,eff}} + H_{\text{FC,eff}} \\
= {}& E_{\eta_0,v_0,S_0} + B_0(\boldsymbol{J} - \boldsymbol{L} - \boldsymbol{S})^2 - D_0[(\boldsymbol{J} - \boldsymbol{L} - \boldsymbol{S})^2]^2 \\
& + D_1[\langle\eta_0\Lambda|\, L_+\, |\eta\Lambda - 1\rangle \langle\eta\Lambda - 1|\, L_+\, |\eta_0\Lambda - 2\rangle\, (J_- - S_-)(J_- - S_-) \\
& + \langle\eta_0\Lambda|\, L_+\, |\eta\Lambda - 1\rangle^2\, (J_- - S_-)(J_+ - S_+) + \langle\eta_0\Lambda|\, L_-\, |\eta\Lambda + 1\rangle^2\, (J_+ - S_+)(J_- - S_-) \\
& + \langle\eta_0\Lambda|\, L_-\, |\eta\Lambda + 1\rangle \langle\eta\Lambda + 1|\, L_-\, |\eta_0\Lambda + 2\rangle\, (J_+ - S_+)(J_+ - S_+)] \\
& + \frac{2}{3}\lambda\left(3S_z^2 - \boldsymbol{S}^2\right) + A\boldsymbol{L}\cdot\boldsymbol{S} + \gamma\boldsymbol{R}\cdot\boldsymbol{S} + \sum_\alpha b_F^\alpha \boldsymbol{S}\cdot\boldsymbol{I}_\alpha. \quad (2.4)
\end{aligned}
$$

The derivation and the physical meaning of the different terms is discussed thoroughly in chapters 4 and 5 of the thesis. The matrix form of the effective Hamil-

tonian is derived and given in section 5.3 of the thesis

$$
\begin{bmatrix}
\ddots & \ddots & 0 & 0 \\
\ddots & H_{J,J} & H_{J,J+1} & 0 \\
0 & H_{J+1,J} & H_{J+1,J+1} & \ddots \\
0 & 0 & \ddots & \ddots
\end{bmatrix}
\tag{2.5}
$$

where $H_{J,J}$ is a 5x5 block, which is the sum of the fine structure effective Hamiltonian matrix (5.75, thesis) for a given J and the diagonal block of the Fermi-contact interaction matrix $H_{\mathrm{FC}}^{J,J}$ (5.90, thesis):

$$
\begin{bmatrix}
\begin{matrix} E'_\Pi + B'_\Pi[J(J+1)-1] \\ +D_\Pi[J(J+1)-1]^2 \end{matrix} & 0 & \eta\sqrt{\frac{J+1}{2J+1}} & \eta\sqrt{\frac{J}{2J+1}} & 0 \\
0 & \begin{matrix} E'_\Pi + B'_\Pi[J(J+1)-1] \\ +D_\Pi[J(J+1)-1]^2 \\ +qJ(J+1) \end{matrix} & 0 & 0 & \eta \\
\eta\sqrt{\frac{J+1}{2J+1}} & 0 & \begin{matrix} E'_\Sigma + B'_\Sigma J(J-1) \\ +D_\Sigma[J(J-1)]^2 \\ -\left(\frac{J-1}{2J+1}\right)\frac{2}{3}\lambda + \gamma(J-1) \\ \frac{1}{2J}[F_1(F_1+1) \\ -J(J+1)-I_1(I_1+1)]K_1 \end{matrix} & \frac{\sqrt{J(J+1)}}{2J+1}2\lambda & 0 \\
\eta\sqrt{\frac{J}{2J+1}} & 0 & \frac{\sqrt{J(J+1)}}{2J+1}2\lambda & \begin{matrix} E'_\Sigma + B'_\Sigma(J+1)(J+2) \\ +D_\Sigma[(J+1)(J+2)]^2 \\ -\left(\frac{J+2}{2J+1}\right)\frac{2}{3}\lambda - \gamma(J-2) \\ -\frac{1}{2(J+1)}[F_1(F_1+1) \\ -J(J+1)-I_1(I_1+1)]K_1 \end{matrix} & 0 \\
0 & \eta & 0 & 0 & \begin{matrix} E'_\Sigma + B'_\Sigma J(J+1) \\ +D_\Sigma[J(J+1)]^2 \\ +\frac{2}{3}\lambda - \gamma \\ \frac{1}{2J(J+1)}[F_1(F_1+1) \\ -J(J+1)-I_1(I_1+1)]K_1 \end{matrix}
\end{bmatrix}
\tag{2.6}
$$

while the off-diagonal block $H_{J,J+1}$ is given only by the Fermi-contact interaction

matrix $H_{\mathrm{FC}}^{J,J+1}$ (5.91, thesis):

$$
\begin{bmatrix}
0 & 0 & 0 & 0 & 0 \\
0 & 0 & 0 & 0 & 0 \\
0 & 0 & 0 & 0 & 0 \\
0 & 0 & 0 & 0 & \begin{array}{c} \frac{1}{2(J+1)}\left[\frac{J+2}{2J+3}\right]^{\frac{1}{2}}[(F_1+I_1+J+2) \\ \times(I_1+J+1-F_1)(F_1+J+1-I_1) \\ \times(F_1+I_1-J)]^{\frac{1}{2}}K_1 \end{array} \\
0 & 0 & \begin{array}{c} \frac{1}{2(J+1)}\left[\frac{J}{2J+1}\right]^{\frac{1}{2}}[(F_1+I_1+J+2) \\ \times(I_1+J+1-F_1)(F_1+J+1-I_1) \\ \times(F_1+I_1-J)]^{\frac{1}{2}}K_1 \end{array} & 0 & 0 \\
\end{bmatrix}.
$$

$$(2.7)$$

The total matrix is $5(2I_1+1)\times 5(2I_1+1)$ in size, with I_1 the nuclear spin quantum number of the nucleus that has dominant effect on the hyperfine structure. The effect of the second nuclei is neglected. In the case for ^{85}Rb with $I_{\mathrm{Rb}}=5/2$ the matrix is 30x30 in size, while for ^{87}Rb, with $I_1=3/2$ it is 20x20. There are eleven molecular constants involved in the effective Hamiltonian thus obtained: $E_\Pi, B_\Pi, D_\Pi, E_\Sigma, B_\Sigma, D_\Sigma, \eta, \lambda, \gamma, q$ and K_1. E_Π and E_Σ are the vibronic energies for the $B^1\Pi$ and $c^3\Sigma^+$ electronic states, respectively. B_Π and B_Σ are their rotational constants, while D_Π and D_Σ are the centrifugal distortion ones. η, λ and γ are the fine structure spin-orbit, spin-spin and spin-rotation interactions respectively. q is the Λ-doubling parameter and finally K_1 is the Fermi-contact interaction constant. Values of these molecular parameters are found thereafter by means of non-linear numerical fit using the experimental data.

Chapter 3

The Experiment

KRb molecules were produced in a stainless steel heat pipe in approximately 1:1 mass ratio of the ingredients in natural isotopic composition, which for potassium is: ^{39}K(93.3%), ^{40}K(0.01%), ^{41}K(6.7%); and for rubidium: ^{85}Rb(72.2%), ^{87}Rb(27.8%). ^{40}K with its approximately 0.01% occurrence is of negligible importance for the experiments here. Most of the lines in the spectra[1] (including in this number the stronger ones) were due to ^{39}K^{85}Rb, ^{39}K^{87}Rb, ^{41}K^{85}Rb, ^{39}K$_2$ and ^{39}K^{41}K. Potassium and rubidium as alkali metals react vigorously with water and oxygen. Using a heat pipe [68–70] is one way to create appropriate environment for production of molecules in gaseous phase in order to investigate the internal molecular structure. Another way to produce alkali molecules is by a molecular beam [71–74]. Both methods come with their pros and cons and are somewhat complementary. The temperature in the heat pipe is a few hundred degrees Celsius and higher vibrational and rotational levels of the ground electronic state are thermally populated, while the temperature in the molecular beam is far lower ($\sim$ 5-20 K) and only few rotational levels of the lowest vibrational state are populated. The spectra from the molecular beam are therefore simpler and more susceptible to interpretation while those from the heat pipe are much more complex. However the abundance of thermally populated levels allows for the investigation of excited states that cannot be reached in the molecular beam. Moreover the collisions that occur in the heat pipe could be used as an advantage to populate adjacent levels through collision transfer. This is particularly suitable for Laser induce fluorescence [23] and in some cases even for Optical-optical double resonance polarization spectroscopy [25], by making the spectra much richer. In other situations it can be a drawback when one does not want such population transfer to occur as is in our case. The presence of collisions will also lead to broadening of the lines, which will

---

[1]Lines from ^{85}Rb$_2$ and its isotopologues were not observed, even though they are expected to absorb in the spectral region covered by the experiments in this work. The reason for this should be searched for in the mass ration of the ingredients, that turns out to determine the concentration of the different diatomic molecules K$_2$, KRb and R$_2$.

lower the resolving power. On the other hand, inside the beam collisions would rarely occur, therefore neither collision transfer nor collision broadening would be observed, but transition line broadening instead. By collimating the molecular beam the first order Doppler broadening is greatly suppressed, while within the heat pipe molecules are free to move in all directions. The Doppler broadening in the latter case has to be overcome by means of saturation spectroscopy, polarization spectroscopy etc. The setup for molecular beam is generally more expensive and involved to be build. It requires also to be continually loaded with ingredients. Contrary, the heat pipe is cheaper and less intricate to build and sustain, and one load will last for hundreds of hours of operation. In previous studies for NaK [75] and NaRb [76] the molecular beam was used in order to investigate the hyperfine structure of their $c^3\Sigma^+$ state. But based on what has just been said we have chosen to start by using the heat pipe and we were able to accomplish our goals, though probably somewhat better results could have been obtained by using a molecular beam, however at much higher cost and experimental efforts.

3.1   The heat pipe

A sketch of the longitudinal cross section of the heat pipe can be seen in figure 3.1. Its way of work is by no mean obvious and easily quantified, for this is a whole separate branch of investigation [77]. Our aim here is to make a brief outline of the device used in this study. The core element is a stainless steel pipe approximately 60 cm in length and 3 cm in diameter. Brass coolers supporting transparent, anti-reflection coated mirrors are mounted on both ends of the pipe. They are cooled by a constant water flow through channels inside them. A heater surrounds the middle part of the pipe and is used along with thermocouple and a PID (proportional-integral-differential) controller to stabilize the temperature at a desired value. A fine stainless steel mesh grid (about 40 cm in length) is placed on the inner surface of the pipe. The pipe is also connected through a valve to a vacuum system composed manly of a rotational vacuum pump, pressure gauge and an argon bottle.

The heat pipe operates as so: metals ($\sim$5 g of Rb and $\sim$5 g of K) are placed inside the pipe; the air is pumped out and the volume is filled with argon as a buffer gas to low pressure (few Torr). The valve is closed, water cooling is turned on, and the heater is set to stabilize the temperature at a preset value. While heating, some of the material will evaporate thus forming free atoms and molecules. The melting point of potassium is 63.5 °C and its boiling point is 758 °C, while for rubidium they are 39.3 °C and 688 °C, respectively. But instead of expanding throughout the whole volume, the molecules will condense on the mesh by getting closer to the ends of the pipe, because of the lower temperature there, and because
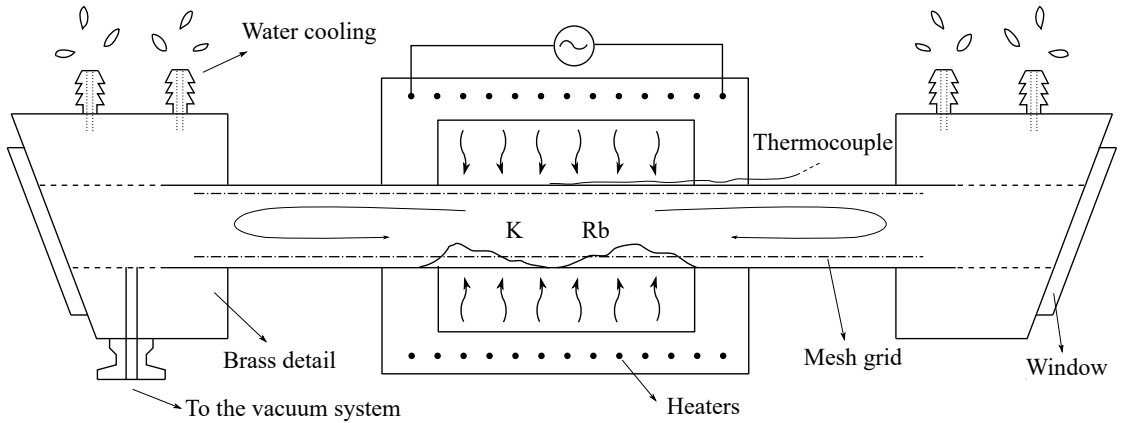
Figure 3.1: Basic longitudinal cross section sketch of the heat pipe.

of collisions with cold Ar atoms, which is the main purpose of the buffer gas; not to let any molecules go near the windows. Here the mesh grid becomes so important, because the material that condenses on it will be driven towards the center of the pipe by capillary forces, along the increase of the temperature, and in this way closing the working cycle. Depending on the working temperature, once the heat pipe is loaded it can serve for many hundreds of hours. Once heated it can also sustain working conditions for more than a dozen of hours. There are two major physical quantities, namely pressure of the argon and the temperature, that can be altered so as to obtain optimal results (spectra). With the setup just described only initial argon pressure can be measured at room temperature, i.e. before the heaters were turned on, and in our case for saturation spectroscopy it was chosen to be 0.5 Torr, while the temperature was finally selected to 280 °C, but more on that will be said later.

3.2 The Laser

As a light source a diode laser (HL6544FM, 50 mW from Thorlabs) with extended cavity was used, working in one mode continuous-wave regime and producing beam with a FWHM of less than 5 MHz. There are three major quantities we can control: the laser temperature, its current and the grating inclination. The temperature was stabilized at about 30.0 °C with a homemade temperature controller designed for that purpose. It was not the precision of the absolute value, but rather its stability in tame that was important in order to maintain stable output frequency. The controller was able keep constant temperature within 200 μK for hours. Controlling the frequency by changing the temperature is a rather slow operation, not so convenient and precise as changing the current, when speaking of diode lasers. Tunning of the frequency was done by a modulating the diode current with a

15

triangular signal ($\approx$ 20 s period). The extension of the cavity was done by placing additional diffraction grating [78]. Without such a supplement the FWHM of the beam would be about 50 MHz, already above the natural linewidth (10-20 MHz). Yet another disadvantage, though the gain of the active media covers a few nm, is that not all frequencies are accessible to be scanned continuously because of mode hopping. The use of the dispersive element in the laser resonator would narrow the FWHM of the output beam and would allow us to scan over the wanted region, but in order to maintain continuous frequency scan it would require synchronous rotation of the grating with the change of the diode current. A piezoelement, driven by high voltage, made this possible so as to obtain mode hop free ≈ 0.8 cm^{-1} scans. To change the frequency region either a course change of the current or a tiny rotation of the diffraction grating, by a fine thread screw supporting the construction, was done. In that way a range of the KRb $B(v' = 2)$ - X($v'' = 0$) band, $15100 - 15140$ cm^{-1}, was covered by overlapping scans.

3.3 Calibration of the spectra

For calibration of the spectrum, Doppler-limited absorption of the iodine dimer in a glass cell was monitored, simultaneously with the recorded spectra, on an oscilloscope, along with the fringes from a confocal interferometer (CFI) with a free spectral range of 748 $\pm$ 1 MHz. The I$_2$ spectrum should in principle be enough for calibration, but normally there would be only a few absorption lines in one scan and this is one reason why the CFI was needed. The laser frequency is also not necessarily linearly scanned throughout the whole scan, due to the use of piezoelement and this is the second reason. Because the fringes are equally spaced in the frequency domain it will improve the accuracy of the calibration. Indeed, one can think of the iodine cuvette as serving the purpose of absolute calibration, while the CFI for relative one. The iodine dimmer is well studied and an atlas is can be found in [79]. The precise technical way for calibration of the spectra is done by means of a linear least-square fit, after finding the peaks of the I$_2$ lines and that of the CFI fringes. A wavemeter (WS5 model) with 0.1 cm^{-1} absolute accuracy, was not suitable for calibration of the spectrum, because precision of the order of 0.001 cm^{-1} was necessary. Nevertheless the instrument was helpful in finding roughly the desired frequency region during setup.

3.4 Saturation spectroscopy

Initially Doppler-free saturation spectroscopy was employed. The experimental setup is shown in figure 3.2. Before entering the heat pipe the beam, now attenuated to about 10 mW, mainly because of imperfections in the mirrors, was
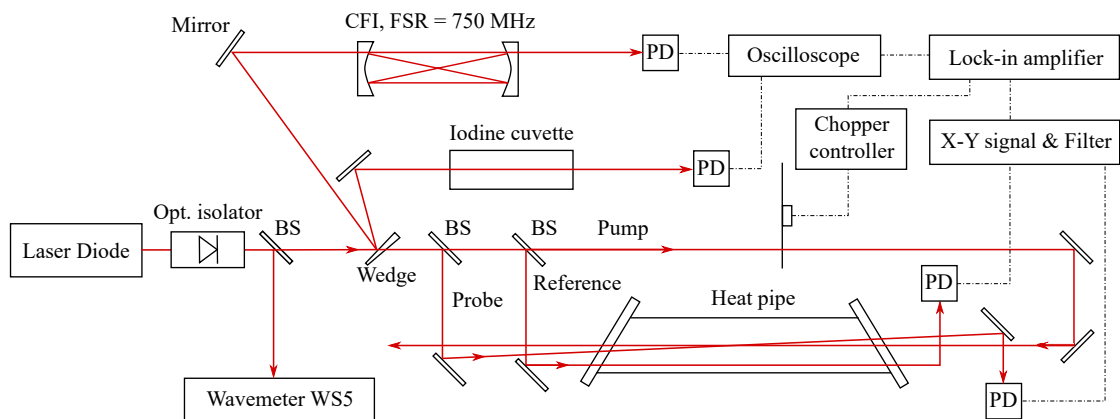
Figure 3.2: Experimental setup for Saturation spectroscopy. CFI stands for Confocal interferometer, FSR - free spectral range, PD - photodiode, BS - beam splitter.

split into two parts - pump and probe, with an intensity ratio of 9:1 respectively. The two beams entered the heat pipe in opposite directions and were overlapped in its center. The absorption of the probe was registered by a photodiode (PD, BPW34). Thus an absorption spectrum with rather weak Lamb dips was observed. To increase the sensitivity a few more things were added. First the intensity of the pump beam was modulated by a mechanical chopper at 6 kHz and the absorption of the probe was registered through a lock-in amplifier (Stanford Research System SR830). But since the signal from the photodiode was of the order of volts, while the useful signal was of the order of millivolts, this would not allow us to apply great amplification before reaching saturation of the instrument. For that reason the pump was once again split and the extracted beam, was used to monitor pure absorption signal, so to serve as a reference. The difference between the probe and the reference signals was send through an electronic band pass filter, whose output then entered into the lock-in amplifier. By taking the difference of the signals any in-phase noise would also be eliminated.

After obtaining signal as strong as possible, there are sill a couple of experimental conditions which need optimization. Because our goal was to observe the hyperfine splitting which, based on previous studies for NaK [75] and NaRb [76], was expected to be of the order of tens or hundreds of MHz, we aimed towards achieving maximum resolving power. There are four main categories to consider concerning line broadening: natural, collision, power and Doppler broadening. (1) Natural line broadening is caused by the interaction of the molecule with the quantum vacuum leading to spontaneous emission and cannot be overcome. For molecules it is typically 10-20 MHz in the visible spectral range and is what can be achieved at best. (2) To minimize collision broadening one has to minimize the frequency of collisions between the particles in the media and in the heat pipe,

the temperature and the pressure of the argon are responsible for that. The following things were considered while searching for optimum values: concerning the Ar pressure, value as low as possible is desired, because an increase would only lead to more collisions. Since the purpose of the argon is to keep the molecules away from the windows, we did not go below 0.5 Torr. If the temperature was bellow 250 °C the molecular concentration would be low and the absorption would be negligible, therefore hard to register; but if the temperature was higher than 330 °C almost a hundred percent absorption would be observed. With increase of the temperature the collision frequency between Ar-KRb, K-KRb, Rb-KRb etc. will increase and the lines would also become broader. A compromise value in this range was then searched for, so as to minimize line broadening and still have strong enough signals. That is how the above mentioned values (0.5 Torr and 280 °C) were obtained [2]. (3) To reduce the power broadening of the lines the intensities of the pump and the probe were altered. It turned out that reducing the pump, the probe, or both of them would not increase the resolving power. Because of that we worked with the whole available power. (4) To reduce any residual Doppler broadening the crossing angle between the pump and the probe was made as low as possible ($< 0.5°$). Finally we add one additional remark concerning transit-time broadening. The beam width was about $w = 2$ mm and the mean velocity of the molecules: $\bar{v} = \sqrt{8kT/\pi m} \approx 300$ m/s. The transit-time FWHM [78] is then estimated be $\delta\nu \approx \bar{v}/w = 60$ kHz, which is negligible in comparison with the natural linewidth.

After optimization of the experimental conditions it was possible to reduce the widths of the unperturbed lines down to about 50 MHz. In [80], where NaK had been prepared in heat pipe (0.5 Torr, 550 K) the researchers reported the have obtained 50 MHz FWHM. They employed Perturbation facilitated polarization spectroscopy. In [81] for NaRb (1 Torr, 600 K of the heat pipe) the linewidths are reported to be 75 MHz, using polarization spectroscopy. In comparison with molecular beam the authors in [75] and [76] reported to have accomplished 20 MHz resolving power. Part of our spectrum is shown in figure 3.3 (upper trace). The saturated spectroscopy spectra were very complex to analyze due to the presence of strong K_2 and KRb $B - X$ bands in multiple isotopologues. There were more than fifty lines per 1 cm^{-1} on average. Nevertheless, it was possible to assign most

---

[2]In thermal equilibrium Boltzmann distribution is established, meaning that the probability of an eigenstate with energy E to be populated is proportional to $\exp\left\{-\frac{E}{kT}\right\}$. To estimate the extend to which the terms are thermally populated we can use as a characteristic value, the energy, that makes the power of the exponent equal to one. For $T = 280$ °C it is 384.5 cm^{-1}. Using also the ground state potential for $^{39}K^{85}Rb$ from [23] it can be calculated that: $E(v'' = 4, J'' = 0) = 336.6$ cm^{-1}, $E(v'' = 5, J'' = 0) = 410.1$ cm^{-1}, $E(v'' = 0, J'' = 95) = 382.0 cm^{-1}$. Even without considering degeneracy of the states or Frank-Condon factors, this information can give as a hint about the manifold of possibility of transitions that can occur at such a temperature.
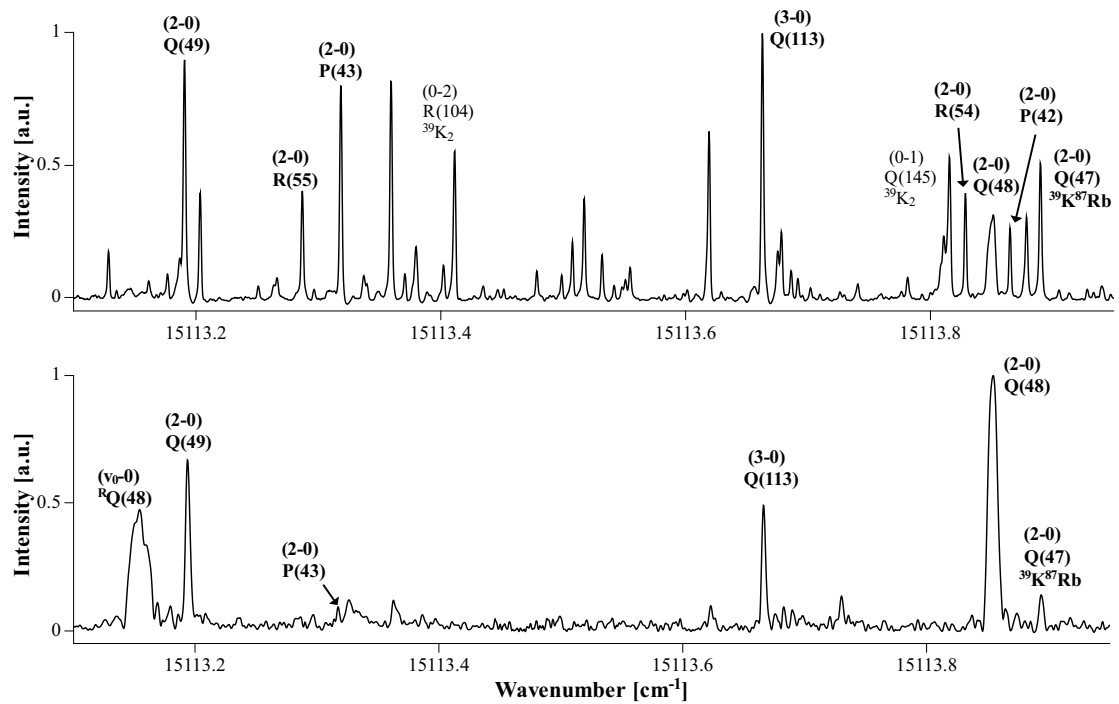
Figure 3.3: Part of the spectrum form saturation spectroscopy (upper trace) and filtered laser excitation spectroscopy (lower trace). Assignments of some transitions are shown above the lines. Broadening due to the HFS is visible for example for the perturbed $(2-0)B - X$ $Q(48)$ transition (compare with $P(43)$ or even $Q(49)$) and for the $(v_0 - 0)c - X$ $^R Q(48)$ transition.

of the strong and non-overlapping transitions, for much of them have already been observed and accurate molecular constants are available in [26, 82][3].

The hyperfine interactions result in broadening and sometimes in splitting of observed spectral lines to the $c^3\Sigma^+$ state (see figure 3.4). In our case outside the regions of perturbation the transitions to the $B^1\Pi$ were not broadened, but when the coupling to the c state becomes strong - the transitions to the B state also show broadening. Due to the dense spectra in saturation spectroscopy the lines with visible HFS, frequently overlap with other lines and the effect of the HFS cannot be fully resolved. Transitions to the $c^3\Sigma^+$ are also with relatively low intensity. Because of that we were not able to identify some of the transitions, measure some of the line widths or to tell to the positions of separate HFS components. That is why Filtered Laser Excitation, Laser Induced Fluorescence and Optical-optical Double Resonance Saturation spectroscopy were additionally used. These techniques are described in chapter 7 in the thesis and helped to assign even more transitions and to measure the broadening or splitting of the HFS.

3.5 Experimental results

In total 130 transitions related to ^{39}K^{85}Rb and 118 transitions related to ^{39}K^{87}Rb were assigned in the saturated spectroscopy and OODRSS spectra. Most of them are transitions to the $B^1\Pi$ state. Term energies of the excited states were obtained by adding the transition frequencies to the ground state term values, which were calculated using the potential energy curve from [23]. This potential is reported to reproduce the experimental data with an estimated uncertainty better than 0.003 cm^{-1}. This turns out to be the main source of uncertainty of the present term values. The uncertainty of the transition frequencies from this study was estimated by comparing 135 frequencies of selected $B - X$ lines of K$_2$, which appear in the saturation spectroscopy spectra (e.g. R(104) in Figure 3.3) with their values from [82]. The root-mean-square (rms) deviation was about 0.001 cm^{-1}. Therefore the combined uncertainty of the excited terms of the (B, c) complex can be conservatively set to 0.003 cm^{-1}. The full list of the experimental observations may be found in the supplementary materials to [83].

For ^{39}K^{85}Rb 86 terms were obtained (with $J \in [22, 61]$), 6 of which belonged to the $c^3\Sigma^+$ state. 75 terms of the $B^1\Pi$ were already observed in [25]. It was not possible to observe fully resolved line splitting of the HFS for this isotopologue, but

---

[3]There is one side effect of saturation spectroscopy, namely the occurrence of additional lines called crossovers. These are not real molecular transitions and occur just in the middle of two closely spaced (within the Doppler width) lines. This fact, among others, initially made us to consider employing double-resonance technique in addition to saturation spectroscopy. But by inspecting carefully the spectra no such crossovers were found, puzzling enough.
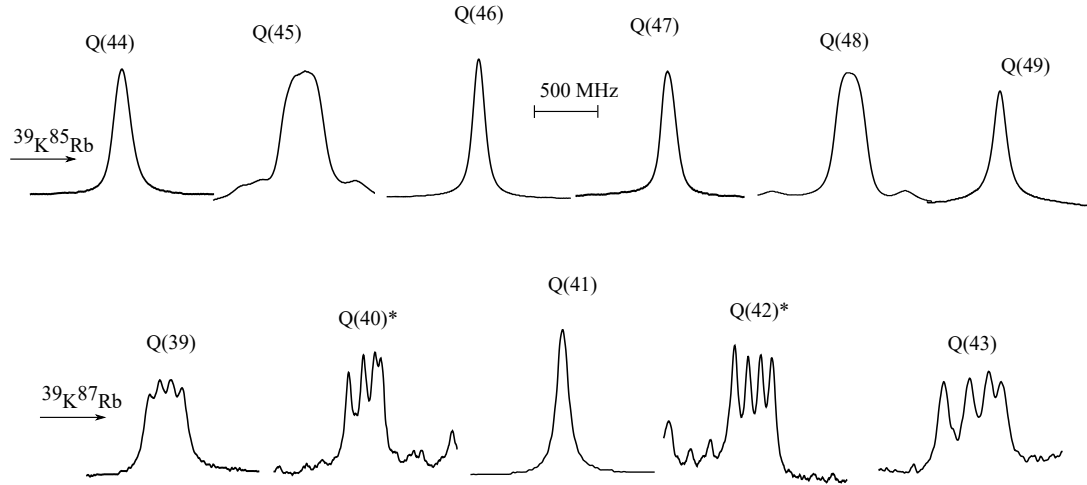
Figure 3.4: On the upper row, $^{39}\text{K}^{85}\text{Rb}$ line shapes for $B^1\Pi(v'=2, J') - X^1\Sigma(v''=0, J'')$ transitions showing broadening due to the interplay between spin-orbit and Fermi-contact interaction. On the lower row, line shapes for some of the $^{39}\text{K}^{87}\text{Rb}$ lines, showing partially resolved splitting. All of the spectra are from OODRSS, except for Q(40) and Q(42) for $^{39}\text{K}^{87}\text{Rb}$ (marked with *) which are from saturation spectroscopy.

only line broadening (figure 3.4, upper row). Linewidths (FWHM) were measured for 11 lines showing such a broadening. For $^{39}\text{K}^{87}\text{Rb}$, 82 terms were obtained (again with $J \in [22, 61]$), 4 belonging to the $c^3\Sigma^+$ state. Splitting of 6 lines into 4 HFS components were identified in the spectra (figure 3.4, lower row). The position of each HFS component was used later in the fit when the nuclear spin effect was taken into account. For the initial fit where only fine structure effects were taken into account, only the central frequency of the HFS was used.

Chapter 4

Results and discussion

A summary of the theoretical model was presented in chapter 2, where the end result was some square matrix that depends on a number of molecular parameters, while the experimental techniques and the data available from them were explained and given in chapter 3. In this chapter the final results from the non-linear least square fit are presented and discussed. More information about the numerical method that is applied and all the details involved can be found in chapter 9 of the thesis.

4.1   The ^{39}K^{87}Rb isotopologue

For the ^{39}K^{87}Rb isotopologue the best fit parameters are given in table 4.1. They reproduce the experimental data with a standard deviation of 0.0014 cm^{-1}, which is already below the estimated experimental uncertainty 0.003 cm^{-1}. We recall from section 3.5, that the uncertainties of the B and c experimental term values was determined, based on the rms for the transitions in our experimental spectra (about 0.001 cm^{-1}) and the estimated uncertainties of the ground state terms (about 0.003 cm^{-1}) from [23]. Apparently the KRb ground state PEC from [23] predicts the term energies more accurately. In figure 4.1 the calculated HFS components relative to their central HFS positions are plotted as a function of J for the $B^1\Pi_f$ state. The experimental data are indicated by an 'X' mark. In figure 4.2 residuals of the term energies are plotted as a function of J. One can see that they are not randomly scattered around the zero line and that there is a cubic-like dependence. Throughout the study we have limited ourselves to the second-order approximation in the effective Hamiltonian method. Normally higher order centrifugal terms will become important for higher J values. But even though it was tried to include the third order term $H[J(J+1)-\Omega^2]^3$ in the model, this cubic-like tendency could not be removed. This is also a reason to find second-order approximation satisfactory enough in our case. The tail for higher J numbers can be explained by the next

	$B^1\Pi(v=2)$	$c^3\Sigma(v_0)$
E	15163.8863(16)	15187.19(36)
B	0.0323594(18)	0.01760(40)
D	$3.799(41) \times 10^{-8}$	$-0.75(11) \times 10^{-6}$
q	$1.36(32) \times 10^{-6}$	
λ		0.4620(48)
γ		0.00386(20)
η	0.4845(10)	
K_1	0.0205(12)	

Table 4.1: Molecular constants and interaction coefficients of the $B^1\Pi(v=2)$ and $c^3\Sigma^+(v_0)$ states in ^{39}K^{87}Rb. All values are in units of cm^{-1}.

center of perturbation around $J' = 70$, which was also partially observed in the spectra, but was not included in the present fit. The correlation matrix of the parameters is given in table 4.2. Along with the uncertainties of the parameters, it is calculated in a standard way, well described in chapter 15.6 of reference [84]. There is a large correlation between the E_Π, B_Π and D_Π molecular parameters, but if we try to exclude D_Π for example, the quality of the final fit will highly degrade and the residuals for higher J values will increase way beyond the experimental uncertainties. The situation with the $c^3\Sigma^+$ state is not quite the same, because there are fewer experimental term energies available. But by keeping D_Σ the fit is somewhat better.

4.2 The ^{39}K^{85}Rb isotopologue

For ^{39}K^{85}Rb, where $I_K = 3/2$ and $I_{Rb} = 5/2$, depending on whether the dominant nuclei would be the potassium or the rubidium one, four or six HFS components had to be expected, respectively. Unfortunately only broadening of the lines was observed for ^{39}K^{85}Rb and the number of the HFS components was not resolved. Later on we will argue that the interaction with the potassium nuclei is very weak and that the Fermi-contact interaction with the rubidium one dominates the broadening of the lines. When taking the Rb nucleus with $I_{Rb} = 5/2$ the corresponding matrix to be diagonalized is 30×30 in size. For completeness we performed also a fit when the main Fermi-contact interaction was assumed to be with the K nucleus ($I_K = 3/2$ and a 20×20 matrix). The raw experimental data for this isotopologue, consist of 11 line widths and 86 term energies. Since only the experimental line widths broadened by the Fermi-contact interaction are available,

$$
\begin{bmatrix}
 & E_\Pi & B_\Pi & D_\Pi & E_\Sigma & B_\Sigma & D_\Sigma & \eta & \lambda & \gamma & K_1 & q \\
\hline
E_\Pi & 1.00 & -0.93 & -0.87 & -0.16 & 0.16 & 0.16 & 0.17 & -0.16 & 0.08 & -0.04 & -0.04 \\
B_\Pi & -0.93 & 1.00 & 0.97 & 0.05 & -0.05 & -0.05 & -0.15 & 0.07 & 0.02 & -0.01 & -0.05 \\
D_\Pi & -0.87 & 0.97 & 1.00 & 0.05 & -0.06 & -0.06 & -0.11 & 0.06 & 0.04 & -0.02 & 0.04 \\
E_\Sigma & -0.16 & 0.05 & 0.05 & 1.00 & -1.00 & -0.98 & 0.02 & 0.78 & -0.39 & 0.17 & 0.09 \\
B_\Sigma & 0.16 & -0.05 & -0.06 & -1.00 & 1.00 & 1.00 & -0.01 & -0.78 & 0.31 & -0.16 & -0.08 \\
D_\Sigma & 0.16 & -0.05 & -0.06 & -0.98 & 1.00 & 1.00 & 0.00 & -0.76 & 0.22 & -0.14 & -0.08 \\
\eta & 0.17 & -0.15 & -0.11 & 0.02 & -0.01 & 0.00 & 1.00 & -0.14 & -0.16 & -0.10 & 0.04 \\
\lambda & -0.16 & 0.07 & 0.06 & 0.78 & -0.78 & -0.76 & -0.14 & 1.00 & -0.30 & 0.08 & -0.03 \\
\gamma & 0.08 & 0.02 & 0.04 & -0.39 & 0.31 & 0.22 & -0.16 & -0.30 & 1.00 & -0.21 & -0.09 \\
K_1 & -0.04 & -0.01 & -0.02 & 0.17 & -0.16 & -0.14 & -0.10 & 0.08 & -0.21 & 1.00 & 0.06 \\
q & -0.04 & -0.05 & 0.04 & 0.09 & -0.08 & -0.08 & 0.04 & -0.03 & -0.09 & 0.06 & 1.00 \\
\end{bmatrix}
$$

Table 4.2: Correlation matrix for the molecular parameter of $^{39}\text{K}^{87}\text{Rb}$.
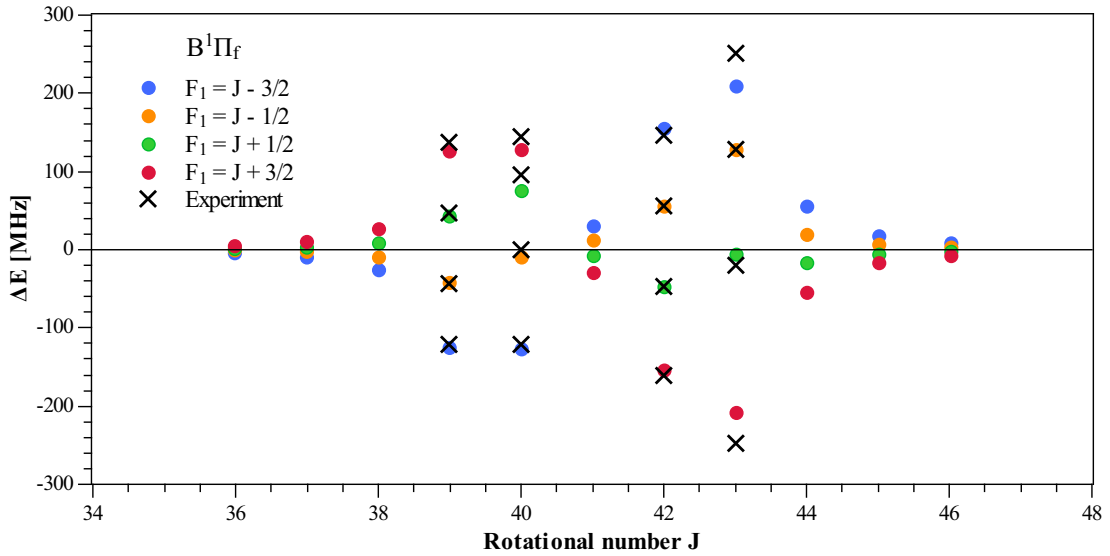

Figure 4.1: Observed and calculated hyperfine splitting of the $B^1\Pi$ state f levels for $^{39}\text{K}^{87}\text{Rb}$ relative to the central position of the corresponding HFS.
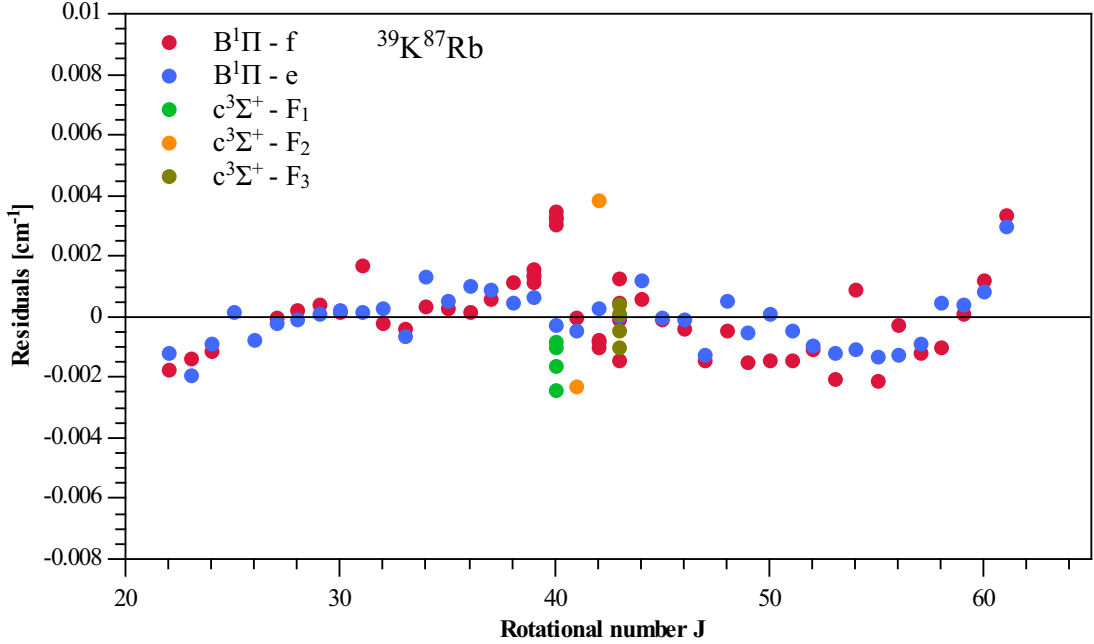
25

Figure 4.2: Residuals of the term energies for $^{39}K^{87}Rb$ as a function of the rotational quantum number (J).

they are compared with a calculated ones. The latter were obtained by adding the apparatus function to each calculated HFS eigenvalue. The apparatus function was defined by a cubic spline fitted to the shape of an unperturbed $B^1\Pi$ line. In this way we assume that the broadening due to the second nuclei does not exceed the apparatus function.

The best fitted parameters from the non-linear fit of the $^{39}K^{85}Rb$ isotopologue are give in Table 4.3. We have performed the fit first with the Rb nucleus, considered to have dominant effect and then with the K one. The molecular parameters describing the fine structure in both cases are virtually the same. Only the hyperfine constant K_1 is different: $0.00560(12)$ cm^{-1} for Rb and $0.00907(20)$ cm^{-1} for K. For both assumptions the rms deviation for the line positions is 0.0022 cm^{-1} and for the line widths: 0.0006 cm^{-1} (≈ 20 MHz). In Figure 4.3 observed and calculated FWHM of the $B^1\Pi_f$ levels are plotted against J for the case where the HFS is modeled with the Rb nucleus. In figure 4.4 residuals of the term energies are plotted as a function of J. Compared with the $^{39}K^{87}Rb$ case (figure 4.2), the same cubic-like pattern is observed but slightly more dispersed in the perturbation region. The tendency is explained again by the next center of perturbation around $J' = 70$. The correlation matrix of the parameters is given in table 4.4. The situation is similar as with $^{39}K^{87}Rb$.

	$B^1\Pi(v=2)$	$c^3\Sigma(v_0)$
E	15164.4343(15)	15193.86(35)
B	0.0325917(18)	0.01678(35)
D	$3.790(42) \times 10^{-8}$	$-0.994(75) \times 10^{-6}$
q	$1.20(33) \times 10^{-6}$	
λ		$-0.2407(34)$
γ		0.00971(8)
η	0.4707(12)	
K_1	0.00560(12)[Rb]	
	0.00907(20)[K]	

Table 4.3: Molecular constants and interaction coefficients of the $B^1\Pi(v=2)$ and $c^3\Sigma^+(v_0)$ states in $^{39}K^{85}Rb$. All values are in units of cm^{-1}.

	E_Π	B_Π	D_Π	E_Σ	B_Σ	D_Σ	η	λ	γ	K_1	q
E_Π	1.00	-0.93	-0.87	-0.09	0.09	0.09	0.09	-0.09	0.07	0.03	0.01
B_Π	-0.93	1.00	0.97	0.03	-0.03	-0.02	-0.02	0.08	-0.07	-0.03	-0.11
D_Π	-0.87	0.97	1.00	0.05	-0.05	-0.05	0.04	0.09	-0.04	-0.03	-0.01
E_Σ	-0.09	0.03	0.05	1.00	-1.00	-1.00	0.05	0.54	0.12	-0.12	0.11
B_Σ	0.09	-0.03	-0.05	-1.00	1.00	1.00	-0.06	-0.55	-0.15	0.12	-0.11
D_Σ	0.09	-0.02	-0.05	-1.00	1.00	1.00	-0.08	-0.56	-0.18	0.13	-0.11
η	0.09	-0.02	0.04	0.05	-0.06	-0.08	1.00	0.00	0.30	0.02	0.02
λ	-0.09	0.08	0.09	0.54	-0.55	-0.56	0.00	1.00	-0.07	-0.19	-0.06
γ	0.07	-0.07	-0.04	0.12	-0.15	-0.18	0.30	-0.07	1.00	-0.11	0.06
K_1	0.03	-0.03	-0.03	-0.12	0.12	0.13	0.02	-0.19	-0.11	1.00	0.01
q	0.01	-0.11	-0.01	0.11	-0.11	-0.11	0.02	-0.06	0.06	0.01	1.00

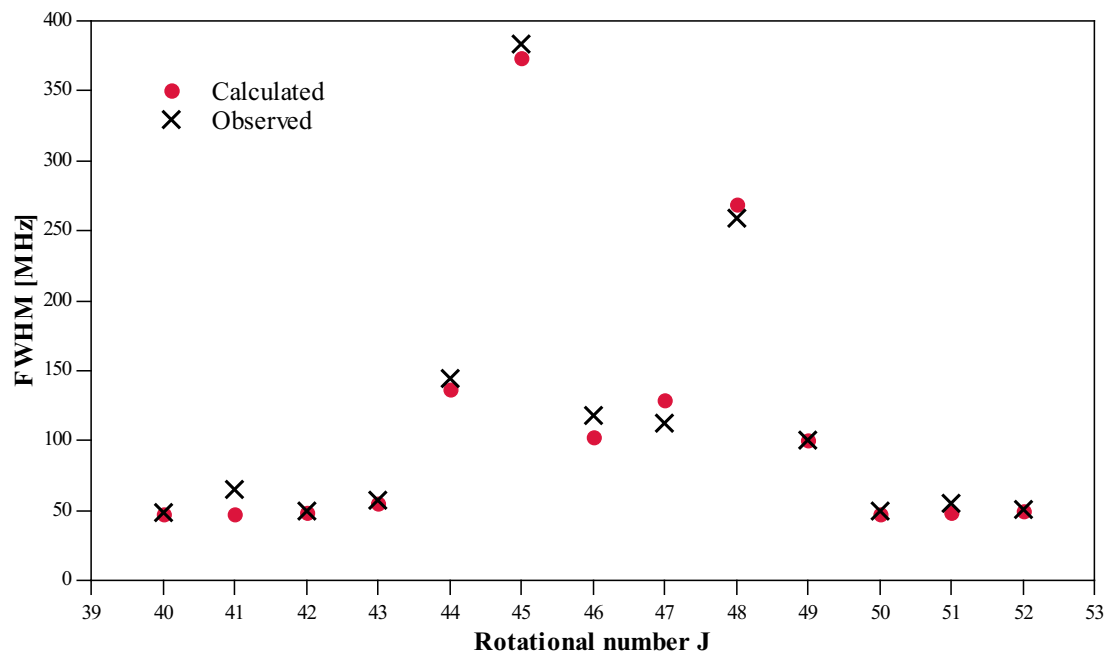Table 4.4: Correlation matrix for the molecular parameter of $^{39}K^{85}Rb$.

Figure 4.3: Observed and calculated FWHM values of transitions to the $B^1\Pi_f(v = 2)$ states are plotted against J for $^{39}\text{K}^{85}\text{Rb}$.
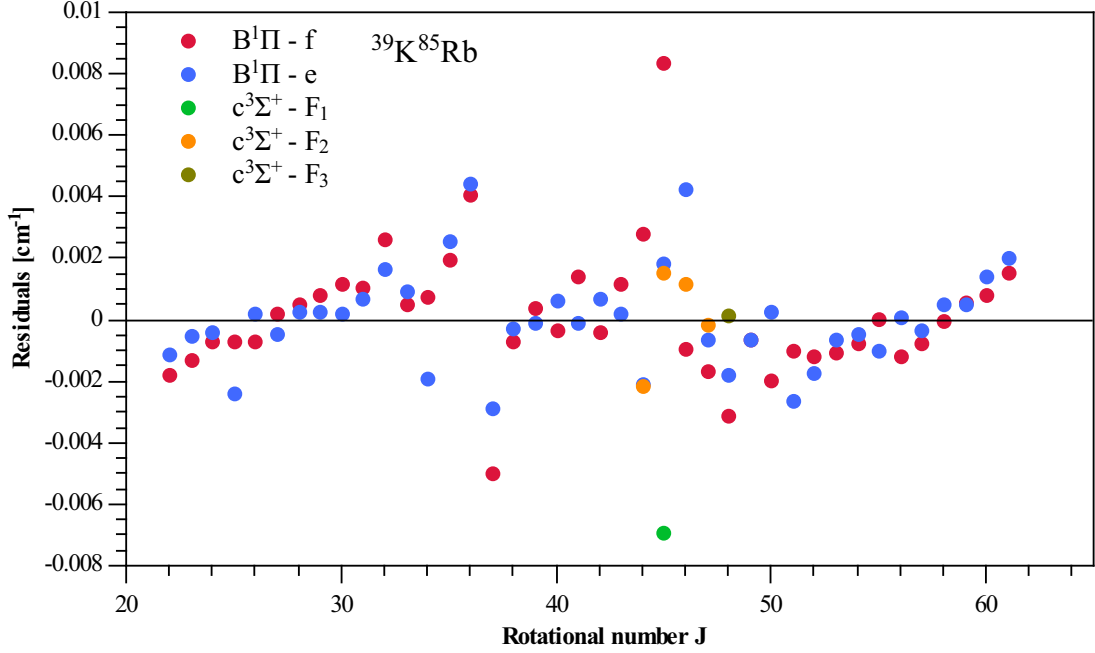
Figure 4.4: Residuals of the term energies for ^{39}K^{85}Rb as a function of the rotational quantum number (J).

4.3 Discussion

Fine structure parameters

To describe the rotational and the fine structure of the $(B-c)$ complex, ten molecular parameters (without K_1) were included in the model: $E_\Pi, B_\Pi, D_\Pi, E_\Sigma, B_\Sigma, D_\Sigma, \eta, \lambda, \gamma$ and q. The E_Π used in the fit is actually the primed constant in equation (5.73, thesis) but for the $B^1\Pi$ state

$$E'_\Pi = E_\Pi + B_\Pi \left\langle L_\perp^2 \right\rangle_\Pi + D_\Pi \left\langle L_\perp^2 \right\rangle_\Pi^2. \tag{4.1}$$

Therefore the fitted parameter is a sum of the electronic and vibrational energies of $(B^1\Pi, v_B = 2)$ plus two small corrections, arising due to non-zero electronic orbital angular momentum perpendicular to the internuclear axis. For of the same reason, the rotational constant B_Π is also corrected. It is given by

$$B'_\Pi = B_\Pi + 2D_\Pi \left\langle L_\perp^2 \right\rangle_\Pi, \tag{4.2}$$

similarly to the primed constant in equation (5.74, thesis). D_Π is the centrifugal distortion constant of the same state. The same considerations apply for E_Σ, B_Σ and D_Σ of the c state. The molecular constants for both isotopologues were determined independently. We decided that this is the proper approach at this stage

29

with limited number of experimental observations. Nevertheless, it is possible to check whether the relationships between the rotational and centrifugal distortion constants can be scaled with the ratio of the reduced masses $\rho = \sqrt{\mu_1/\mu_2}$: $B_2/B_1 = \rho^2$ and $D_2/D_1 = \rho^4$, where the subscripts 1 and 2 refer to $^{39}\text{K}^{85}\text{Rb}$ and $^{39}\text{K}^{87}\text{Rb}$, respectively. In the case of the study $\rho \approx 0.996378$ [85]. For the $B^1\Pi$ state, $B_2/B_1 = 0.992871(78)$ and $\rho^2 = 0.992771$, which gives a 1.3σ difference. The ratio of the centrifugal distortion constants is $D_2/D_1 = 1.002(15)$ and $\rho^4 = 0.986$, which is a 1.1σ difference. So for the B state these relationships can be considered fulfilled. For the $c^3\Sigma^+$ state however, the ratio of the rotational constants is $B_2/B_1 = 1.049(30)$, which is 1.9σ away from the expected value of ρ^2. The fitted centrifugal distortion constants are with opposite, negative signs, most probably due to the smaller number of experimental data available for the $c^3\Sigma^+$ state. They therefore deviate from their original physical meaning and serve only as effective parameters in the fit.

The effect of the Lambda doubling on the $B^1\Pi$ state is described by the term $qJ(J+1)$. The parameter q is given by equation (5.54, thesis) and takes into account the balanced second order rotational interactions of $B^1\Pi$ with $A^1\Sigma^+$ and $C^1\Sigma^+$. The value for the fitted parameter q is very small (see tables 4.1 and 4.3). In fact the splitting between the e and f components was discovered only at the end of the study, when the residuals of the fits were plotted. Such small splitting is observed in the analogous $B^1\Pi$ states in the mix alkalies, e.g. NaK [75] and NaRb [76].

The spin-orbit, spin-spin and spin-rotation coupling constants - η, λ and γ, as discussed in section 4.7.2 in the thesis, all incorporate first and second order effects

$$\eta = \eta^{(1)} + \eta^{(2)}, \tag{4.3}$$

$$\lambda = \lambda^{(1)} + \lambda^{(2)}, \tag{4.4}$$

$$\gamma = \gamma^{(1)} + \gamma^{(2)}, \tag{4.5}$$

where the first order contributions are given by equations (5.64, 4.104, 4.106, thesis). The value for the spin-rotation constant γ may be compared with the value from [29], although the analysis there covers only the first 14 vibrational levels of the $c^3\Sigma^+$ state. Recently the same experimental data were reanalyzed within a new coupled channels model [62], where ab initio calculations provided the missing R-dependent matrix elements. In table III from ref. [29] for $v'_c = 0$ $\gamma = 0.00166(4)$ cm^{-1} with a pronounced decrease with v_c. It is unsafe to extrapolate this value to $v_c = 37 - 40$ which is the most probable perturber of the $v_B = 2$ in the B state. In [62] the pure spin-rotation γ is 3.3×10^{-4} cm^{-1}, however one should add to it the second order corrections which are a factor of 2-3 times larger. Nevertheless, these values are significantly smaller than those from our analysis: $\gamma = 0.00970(7)$ cm^{-1} for $^{39}\text{K}^{85}\text{Rb}$ and $\gamma = 0.00386(20)$ cm^{-1} for $^{39}\text{K}^{87}\text{Rb}$.

In [29] an estimate for the spin-spin interaction is given, $\epsilon = -0.469(2)$ cm^{-1} (Amiot used a different notation for this parameter). The order of magnitude is the same as for λ from table 4.3. For ^{39}K^{87}Rb the sign is opposite and we found out that this was crucial for the present experimental observations.

The first order part of the spin-orbit interaction is the average value of the off-diagonal spin-orbit function, $\langle v_B | \xi_{Bc}(R) | v_c \rangle$. In reference [62] a theoretical function for $\xi_{Bc}(R)$ is published and it can be used to estimate the value of $\eta^{(1)}$. In the same paper the authors report a refined ab initio $c^3\Sigma^+$ potential by using the low v_c experimental data from [29]. In ref. [61] adiabatic potential for the $B^1\Pi$ state can be found based on the experimental data from [35]. Ab initio calculations on the $B^1\Pi$ and $c^3\Sigma^+$ state PECs are reported also in [53, 63]. The estimates for $\eta^{(1)}$ based on these three pairs of potentials are 3.7 cm^{-1}(PECs from [61, 62]), 0.32 cm^{-1} ([63] PECs) and -0.12 cm^{-1} ([53] PECs). The B state potential from [61] should be considered as the most accurate so far, however the c state [62] has a very steep repulsive branch and this results in an overestimated overlap with the $v_B = 2$ level in $B^1\Pi$ state. The values of the $\eta^{(1)}$ from the ab initio potentials seem more consistent and the deviations come mainly due to different positions of the $B - c$ crossing.

All of the above mentioned discrepancies indicate that the second order contributions in the fine structure parameters are also important. The fitted molecular parameters reproduce the experimentally observed term energies within the uncertainties, but in order to say more about their physical significance either more experimental data is needed, or a more general coupled channels model, which includes the $B^1\Pi$, $c^3\Sigma^+$ and possibly $C^1\Sigma^+$ states, has to be considered.

Hyperfine structure parameters

We will start the discussion with the ^{39}K^{87}Rb isotopologue, because of the partially resolved hyperfine structure. The nuclear spins are $I_{\mathrm{K}} = 3/2$ and $I_{\mathrm{Rb}} = 3/2$, therefore whichever nuclei is considered to have dominant effect, it is expected to produce splitting of a line to the $c^3\Sigma^+$ state into four main HFS components, as observed in the experiment (figure 4.5). That the observed splitting is mainly due to the interaction with the rubidium nuclei, follows from the fact that the HFS splitting changes significantly when changing the Rb isotope (see figure 3.4). The effect of the second nucleus apparently is very small and leads only to broadening of the hyperfine components within the resolution of the present experiment. It is a situation similar to the HFS of the $c^3\Sigma^+$ in NaK [75], where the Fermi-contact interaction with the sodium nuclei dominates and the interaction with K leads only to additional broadening of the main hyperfine components. For our case, in figure 4.5 one can compare the line widths of the hyperfine components of the $(v' = 2, J' = 40, F_1)$ $c^3\Sigma^+$ level $(170 \pm 30$ MHz$)$ with an unperturbed transitions to
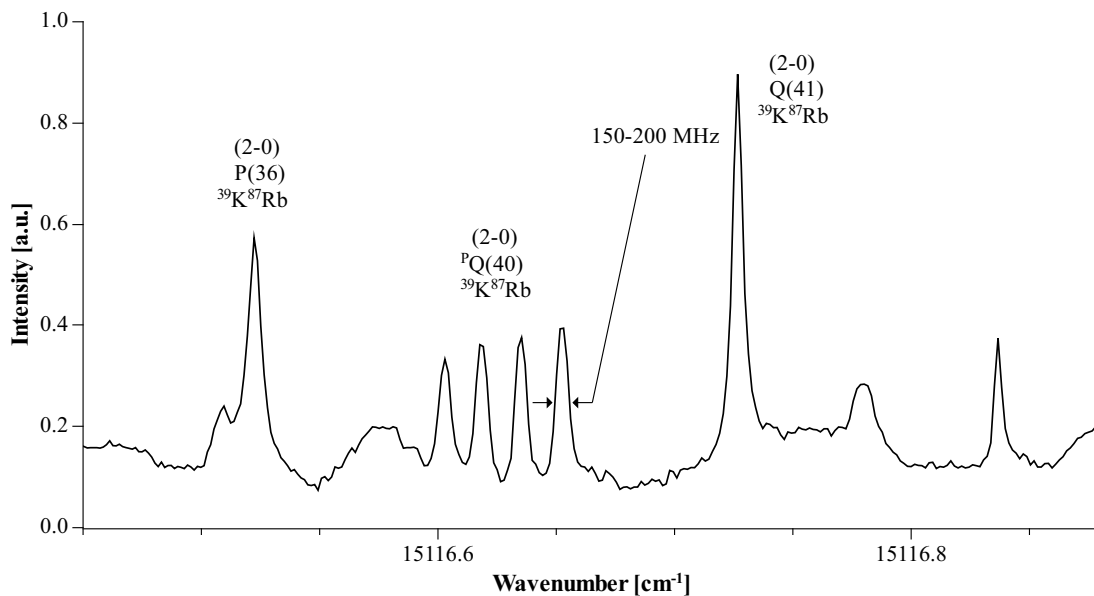
Figure 4.5: Recorded spectrum with OODRSS. The pump laser was fixed on the $X(v'' = 0) - B(v' = 2)$, P(40) transition of ^{39}K^{87}Rb, so as to label the $v'' = 0, J'' = 40$ ground state.

the $B^1\Pi$ state (about 90 MHz). This extra broadening allows us to estimate the splitting of the hyperfine components due to the second nucleus. The calculation is done in somewhat similar way as with the linewidths for ^{39}K^{85}Rb. There we had six lines, each covered with an apparatus function to produce the overall line shape, while now we have four lines. The four lines for $J = 40$ and $N = J - 1 = 39$ in figure 4.5 have $F_1 = 38.5, 39.5, 40.5, 41.5$ quantum number. If the experimental resolution was greater each line would have been further decomposed into four components with different F_2 values, e.g. the one with $F_1 = 41.5$ will have $F_2 = 40, 41, 42, 43$. The relative position of these F_2 components can be calculated by using the diagonal matrix element of the Fermi-contact interaction of the second nuclei given in equation (5.92, thesis) for the $N = J - 1$ state, because in first-order approximation the diagonal elements of a perturbation will give the shifts. Then given the relative positions and the apparatus function, the width of the overall line is calculated. This is done for a range of input K_2 values and a scatter plot of the linewidth as a function of K_2 is obtained. From there it is deduced that to have width of 170 ± 30 MHz, K_2 should be equal to 0.0012 ± 0.0003cm^{-1}.

To determine whether one of nuclei has dominant effect in the hyperfine splitting for the ^{39}K^{85}Rb isotopologue and to say which one is it, an additional connection between the atomic and molecular constants of the Fermi-contact interaction, will be used. Such connection can be established through the use of molecular or-

bitals. In diatomic alkali molecules only the two outermost electrons are involved in the bound. The other electrons form closed shells around the two nuclei and do not contribute to the total electronic spin. It is not our purpose here to show how these molecular wave function are constructed out of the atomic ones by linear combinations [65, 86]. The molecular orbital for the $c^3\Sigma^+$ state are

$$|0\rangle |11\rangle = \frac{1}{\sqrt{2}}\Big[|\sigma s(1)\rangle |\sigma p_0(2)\rangle - |\sigma p_0(1)\rangle |\sigma s(2)\rangle\Big] |\alpha(1)\rangle |\alpha(2)\rangle, \tag{4.6}$$

$$|0\rangle |1-1\rangle = \frac{1}{\sqrt{2}}\Big[|\sigma s(1)\rangle |\sigma p_0(2)\rangle - |\sigma p_0(1)\rangle |\sigma s(2)\rangle\Big] |\beta(1)\rangle |\beta(2)\rangle, \tag{4.7}$$

$$|0\rangle |10\rangle = \frac{1}{2}\Big[|\sigma s(1)\rangle |\sigma p_0(2)\rangle - |\sigma p_0(1)\rangle |\sigma s(2)\rangle\Big]\Big[|\alpha(1)\rangle |\beta(2)\rangle + |\beta(1)\rangle |\alpha(2)\rangle\Big], \tag{4.8}$$

with $|\Lambda\rangle |S\Sigma\rangle$ used as notation and where $|\alpha\rangle$ $(m_s = 1/2)$ and $|\beta\rangle$ $(m_s = -1/2)$ are the one electron spin wave functions in the molecule-fixed frame of reference. $|\sigma s\rangle = a\left|4s^{\mathrm{K}}\right\rangle + b\left|5s^{\mathrm{Rb}}\right\rangle$ and $|\sigma p_0\rangle = c\left|4p_0^{\mathrm{K}}\right\rangle + d\left|5p_0^{\mathrm{Rb}}\right\rangle$ are the spatial parts of the molecular orbitals, expressed as linear combinations of the atomic ones, again with respect to the molecular frame. They are also restricted by the normalization conditions

$$a^2 + 2abS_1 + b^2 = 1, \quad S_1 = \left\langle 4s^{\mathrm{K}}|5s^{\mathrm{Rb}}\right\rangle, \tag{4.9}$$

$$c^2 + 2cdS_2 + d^2 = 1, \quad S_2 = \left\langle 4p_0^{\mathrm{K}}|5p_0^{\mathrm{Rb}}\right\rangle, \tag{4.10}$$

with S_1 and S_2, the overlap integrals.

To calculate K_1 defined by equation (5.83, thesis), the reduced matrix element of the operator has to be found. On one side, through the use of the Wigner-Eckard theorem applied to one of the matrix elements we have

$$\langle 0| \langle 10| \zeta_1 \sum_i s_{q,i}^{(1)} \delta(\boldsymbol{R}_1 - \boldsymbol{r}_i) |0\rangle |11\rangle$$

$$= (-1)^{q+1-0} \begin{pmatrix} 1 & 1 & 1 \\ 0 & q & 1 \end{pmatrix} \sqrt{2.1+1}(01||\zeta_1 \sum_i s_i^{(1)} \delta(\boldsymbol{R}_1 - \boldsymbol{r}_i)||01)$$

$$= \frac{1}{\sqrt{2}}(01||\zeta_1 \sum_i s_i^{(1)} \delta(\boldsymbol{R}_1 - \boldsymbol{r}_i)||01) = K_1, \tag{4.11}$$

where the only non-zero term is for $q = -1$, because of the 3-j symbol. On the other side we can calculate the matrix element itself, through the use of the molecular orbitals given in (4.6,4.8). If we take Rb as the first nucleus and K as the second

one, the end result will be

$$
\langle 0| \langle 10| \sum_i s_{q,i}^{(1)} \delta(\boldsymbol{R}_1 - \boldsymbol{r}_i) |0\rangle |11\rangle = \frac{1}{2}\Big[b^2 \left\langle 5s^{\mathrm{Rb}} \left| \delta(\boldsymbol{R}_1)\right| 5s^{\mathrm{Rb}} \right\rangle
$$

$$
+ 2ab \left\langle 5s^{\mathrm{Rb}}\right| \delta(\boldsymbol{R}_1) \left|4s^{\mathrm{K}}\right\rangle + a^2 \left\langle 4s^{\mathrm{K}}\right| \delta(\boldsymbol{R}_1) \left|4s^{\mathrm{K}}\right\rangle + c^2 \left\langle 4p_0^{\mathrm{K}}\right| \delta(\boldsymbol{R}_1) \left|4p_0^{\mathrm{K}}\right\rangle \Big]
$$

$$
- \Big(ac \left\langle 4s^{\mathrm{K}}\right| \delta(\boldsymbol{R}_1) \left|4p_0^{\mathrm{K}}\right\rangle + bc \left\langle 5s^{\mathrm{Rb}}\right| \delta(\boldsymbol{R}_1) \left|4p_0^{\mathrm{K}}\right\rangle \Big)\Big(bc \left\langle 4p_0^{\mathrm{K}}|5s^{\mathrm{Rb}}\right\rangle + ad \left\langle 5p_0^{\mathrm{Rb}}|4s^{\mathrm{K}}\right\rangle \Big)
$$

$$
\approx \frac{1}{2}b^2 \left\langle 5s^{\mathrm{Rb}} \left| \delta(\boldsymbol{R}_1)\right| 5s^{\mathrm{Rb}}\right\rangle, \quad (4.12)
$$

where only the dominant term was left and the others were neglected. Therefore we obtain

$$
K_1 \approx \frac{1}{2}b^2 \zeta_1 \left\langle 5s^{\mathrm{Rb}} \left| \delta(\boldsymbol{R}_1)\right| 5s^{\mathrm{Rb}}\right\rangle. \quad (4.13)
$$

The atomic hyperfine structure constant for the Fermi-contact interaction of the $5s\ ^2S_{1/2}$ state is defined as

$$
A_{\mathrm{Rb}} = \zeta_1 \left\langle 5s^{\mathrm{Rb}} \left| \delta(\boldsymbol{R}_1)\right| 5s^{\mathrm{Rb}}\right\rangle. \quad (4.14)
$$

Hence the connection between the molecular and the atomic constants is in the form

$$
K_{1,\mathrm{Rb}} \approx \frac{1}{2}b^2 A_{\mathrm{Rb}}. \quad (4.15)
$$

In a similar way, for the K nucleus it is derived that

$$
K_{2,\mathrm{K}} \approx \frac{1}{2}a^2 A_{\mathrm{K}}, \quad (4.16)
$$

where

$$
A_{\mathrm{K}} = \zeta_2 \left\langle 4s^{\mathrm{K}} \left| \delta(\boldsymbol{R}_2)\right| 4s^{\mathrm{K}}\right\rangle. \quad (4.17)
$$

In table 4.5 we present a collection of atomic constants A [87] and experimentally determined values for K_1 and K_2 describing the HFS structure of $c^3\Sigma^+$ in NaK [75], Na^{85}Rb [76] and KRb (this study). The values of the coefficients a and b are calculated form (4.15) and (4.16) by substitution of the atomic and the molecular constants. Both of these coefficients must be in the range [0,1] according to the normalization condition. They determine the contribution of the relevant atomic orbital in the constructed molecular one.

For the $c^3\Sigma^+$ states of NaK and NaRb the contribution of the $|3^2S, \mathrm{Na}\rangle$ is dominant, $a = 0.84$ and $a = 0.65$ respectively. In KRb the contribution of both atomic orbitals seems to be comparable. One may speculate that in NaK and NaRb, the $c^3\Sigma^+$ state correlates to an asymptote with Na atom in the ground 3^2S state, and therefore the contribution of this state to the MO is dominant. In KRb,

	A [cm^{-1}]		Mol. HFS const. [cm^{-1}]		a	b	Asymptote
NaK[75]	0.0295	0.0077	0.0105	0.0006	0.84	0.39	(3^2S)Na+(4^2P)K
NaK[88]	0.0295	0.0077	0.0103(2)	$\leq$0.0003	0.83	0.28	(3^2S)Na+(4^2P)K
Na^{85}Rb[76]	0.0295	0.0338	0.0065	0.00013	0.65	0.28	(3^2S)Na+$(5^2P)^{85}$Rb
K^{85}Rb	0.0077	0.0338	0.0012(3)	0.00560(12)	0.56	0.58	(4^2S)K+$(5^2P)^{85}$Rb
K^{87}Rb	0.0077	0.1140	0.0012(3)	0.0205(12)	0.56	0.60	(4^2S)K+$(5^2P)^{87}$Rb

Table 4.5: Atomic [87] and molecular constants for the $c^3\Sigma^+$ state in NaK [75, 88], Na^{85}Rb [76], K^{85}Rb and K^{87}Rb (this study). The sequence of the constants corresponds to the order of the atoms in the molecule.

asymptotically the K atom is in the ground state 4^2S, however the next asymptote $4^2P + 5^2S$ is very close (see figure 2.1) and this may be the reason for the strong mixing of the Rb 5^2S state. We believe that the modern ab initio calculations on the molecular structure can provide reliable estimations of the molecular hyperfine constants, which can be compared with the experimental results from Table 4.5.

We return back to the point which nucleus has dominant effect on the hyperfine structure by the Fermi-contact interaction. While it is clearer for the ^{39}K^{87}Rb isotopologue that the ^{87}Rb nucleus produces the splitting and the K one is responsible for the broadening of each hyperfine components, it is not as evident for the ^{39}K^{85}Rb isotopologue. However, it can be argued that most probably the ^{85}Rb nucleus plays the major role again, for the following reasons: (1) Equations (4.15,4.16) which connect atomic and molecular constants, also set an upper limit for the molecular constant, if we assume in the worst case a or b to be equal to one; i.e. the molecular constant cannot exceed half the atomic one. The derivation of these relations was based upon the use of molecular orbitals, which are only approximations to the real ones, so this restriction is not an absolute upper limit. However, with $A_{\mathrm{K}} = 0.0077$ cm^{-1} and $K_{1,\mathrm{K}} = 0.00907$ cm^{-1} (see Table 4.3) it follows that $a = 1.53$, making it very unlikely that the K nucleus dominates. (2) The ratio between the atomic constants of the Rb isotopes, $A_{^{87}\mathrm{Rb}}(5^2S)/A_{^{85}\mathrm{Rb}}(5^2S) = 0.1140/0.0337 \approx 3.38$ is very close to ratio between the molecular HFS constants from this study $K_{^{87}\mathrm{Rb}}(c^3\Sigma^+)/K_{^{85}\mathrm{Rb}}(c^3\Sigma^+) = 0.0205/0.0056 \approx 3.66(22)$ (where $K_{^{87}\mathrm{Rb}}(c^3\Sigma^+)$ stands for K_1 of K^{87}Rb and similarly for K^{85}Rb). The fitted K^{85}Rb constant can be scaled from the K^{87}Rb constant by the ratio of the atomic ones, so the assumptions that Rb nuclei is dominant in both isotopologues lead to the same value of b, which is expected since the electronic wave function should be nearly invariant with respect to interchange of the Rb isotopes. (3) Because the electronic wave function should be nearly invariant with respect to interchange of the Rb isotopes, we also have to expect that $K_{2,\mathrm{K}}$ would be nearly the same for both isotopologues. However, the value $K_{2,\mathrm{K}} = 0.0012$ cm^{-1} estimated for ^{39}K^{87}Rb is a couple of times smaller than the fitted one $K_{2,\mathrm{K}} = 0.00907$ cm^{-1} for ^{39}K^{85}Rb.

Chapter 5

Summary and Conclusions

In this thesis the results of spectroscopic studies of the KRb molecule are presented. The focus is on a particular perturbation ($v'_B = 2$) between the $B^1\Pi$ and the $c^3\Sigma^+$ electronic states. Rotational terms belonging to the two different states interact because of strong spin-orbit coupling. Other fine structure interactions such as the spin-spin and spin-rotation turned out to play significant role and were necessary to be considered. Furthermore in the perturbation region some transitions to the $B^1\Pi$ state have shown line broadening for the $^{39}K^{85}Rb$ and some - splitting for the $^{39}K^{87}Rb$ isotopologues. This effect is attributed to the interplay between the spin-orbit and Fermi contact interactions, therefore the hyperfine structure effects are considered as well.

An experimental setup is developed and four spectroscopic techniques are employed in this investigation. Two of them: Filtered laser excitation and Laser induced fluorescence spectroscopy are used as supplementary, to assign some of the transitions. The main body of data is coming from the high resolution saturation spectroscopy and from the highly selective optical-optical double resonance saturation spectroscopy. The KRb molecules are produced in a heat pipe and optimal working conditions are obtained for the high resolution Doppler free measurements. In total, 130 transitions and 11 FWHM of lines that show broadening related to $^{39}K^{85}Rb$ were measured and assigned. For $^{39}K^{87}Rb$, 118 transitions were assigned, six of which are split into four HFS components.

The effective Hamiltonian method is used as theoretical model. It takes into account both fine and hyperfine structure effects, and is able of explaining the experimental data within their uncertainties. The model incorporates eleven molecular parameters, values of which are obtained after a non-linear Levenberg-Marquartd numerical fit. Same analysis, but separately, is conducted both for $^{39}K^{85}Rb$ and $^{39}K^{87}Rb$ isotopologues. While the experiment is more definitive about the source of hyperfine splitting in $^{39}K^{87}Rb$, i.e. from the Fermi contact interaction with the ^{87}Rb nucleus, such is not the case with the main isotopologue $^{39}K^{85}Rb$. However, the analysis has shown that most probably, again the ^{85}Rb nucleus has dominant

role. The final results of this study for the molecular constants are presented along with their calculated uncertainties. The physical meaning of the obtained values is also discussed.

One future perspective is to investigate the hyperfine structure of the lowest lying triplet $a^3\Sigma^+$ state. This could be done via optical-optical double resonance saturation spectroscopy in Λ-type configuration, where the $B^1\Pi$-$c^3\Sigma^+$ mixing is used as an intermediate step. Another possibility is to extend furthermore the experimental data to higher v' in the B state and perform more global Coupled-channel deperturbation analysis of the excited electronic states.

Chapter 6

List of author's publications

The main results discussed in this thesis were published in the following papers:

1. V. Stoyanov and A. Pashov. "Investigation on the fine and hyperfine structure of the $c^3\Sigma^+$ state in KRb". *JQSRT* **316**, 108908 (2024).

2. V. Stoyanov and A. Pashov. "Investigation on the fine structure of the $B^1\Pi - c^3\Sigma^+$ complex in KRb". *Journal of Physics: Conference Series* **2710**, 012036 (2024).

Bibliography

[1] C. E. Moore. *Atomic energy levels as derived from the analyses of optical spectra*. **1-3**. US Department of Commerce, National Bureau of Standards.

[2] H. Wang and W. C. Stwalley. "Ultracold photoassociative spectroscopy of heteronuclear alkali-metal diatomic molecules". *J. Chem. Phys.* **108**, 5767–5771 (1998).

[3] W. C. Stwalley and H. Wang. "Photoassociation of Ultracold Atoms: A New Spectroscopic Technique". *J. Mol. Spectrosc.* **195**, 194 (1999).

[4] K. M. Jones, E. Tiesinga, P. D. Lett and P. S. Julienne. "Ultracold photoassociation spectroscopy: Long-range molecules and atomic scattering". *Rev. Mod. Phys.* **78**, 483 (2006).

[5] D. Wang, J. Qi, M. F. Stone, O. Nikolayeva, H. Wang, B. Hattaway, S. D. Gensemer, P. L. Gould, E. E. Eyler and W. C. Stwalley. "Photoassociative Production and Trapping of Ultracold KRb Molecules". *Phys. Rev. Lett.* **93**, 243005 (2004).

[6] D. Wang, J. Qi, M. F. Stone, O. Nikolayeva, B. Hattaway, S. D. Gensemer, H. Wang, W. T. Zemke, P. L. Gould, E. E. Eyler and W. C. Stwalley. "The photoassociative spectroscopy, photoassociative molecule formation, and trapping of ultracold $^{39}K^{85}Rb$". *Eur. Phys. J. D* **31**, 165–177 (2004).

[7] F. Ferlaino, C. D'Errico, G. Roati, M. Zaccanti, M. Inguscio, G. Modugno and A. Simoni. "Feshbach spectroscopy of a K-Rb atomic mixture". *Phys. Rev. A* **73**, 040702(R) (2006).

[8] F. Ferlaino, C. D'Errico, G. Roati, M. Zaccanti, M. Inguscio, G. Modugno and A. Simoni. "Erratum: Feshbach spectroscopy of a K-Rb atomic mixture [Phys. Rev. A 73, 040702 (2006)]". *Phys. Rev. A* **74**, 039903 (2006).

[9] S. Ospelkaus, C. Ospelkaus, L. Humbert, K. Sengstock and K. Bongs. "Tuning of Heteronuclear Interactions in a Degenerate Fermi-Bose Mixture". *Phys. Rev. Lett.* **97**, 120403 (2006).

[10] V. Vitanov K. Bergmann, N and B. W. Shore. "Perspective: Stimulated Raman adiabatic passage: The status after 25 years". *J. Chem. Phys.* **142**, 170901 (2015).

[11] K.-K. Ni et al. "A High Phase-Space-Density Gas of Polar Molecules". *Science* **322**, 231 (2008).

[12] K. Aikawa, D. Akamatsu, M. Hayashi, K. Oasa, J. Kobayashi, P. Naidon, T. Kishimoto, M. Ueda and S. Inouye. "Coherent Transfer of Photoassociated Molecules into the Rovibrational Ground State". *Phys. Rev. Lett.* **105**, 203001 (2010).

[13] J. Kobayashi, K. Aikawa, K. Oasa and S. Inouye. "Prospects for narrow-line cooling of KRb molecules in the rovibrational ground state". *Phys. Rev. A* **89**, 021401(R) (2014).

[14] J. M. Walter and S. Barratt. "The existence of intermetallic compounds in the vapour state. The spectra of the alkali metals, and of their alloys with each other". *Proc. R. Soc. Lond. A* **119**, 257–275 (1928).

[15] E. S. Hrycyshyn and L. Krause. "Sensitized fluorescence in vapors of alkali metals. XI Energy transfer in potassium–rubidium collisions". *Can. J. Phys.* **47**, 215 (1969).

[16] E. S. Hrycyshyn and L. Krause. "Sensitized fluorescence in vapors of alkali metals. XII. $4^2P_{1/2} - 4^2P_{3/2}$ mixing in potassium, induced in collisions with ground-state rubidium atoms". *Can. J. Phys.* **47**, 223 (1969).

[17] M. H. Ornstein and R. N. Zare. "Measured Absolute Cross Sections for K* + Rb Collisional Excitation Transfer". *Phys. Rev.* **181**, 214 (1969).

[18] V. Stacey and R. N. Zare. "Cross-Section Ratios for K*+Rb Electronic Excitation Transfer". *Phys. Rev. A* **1**, 1125 (1970).

[19] R. Beuc, S. Milosevic and G. Pichler. "New diffuse bands in the KRb molecule". *J. Phys. B: Atom. Mol. Phys.* **17**, 739–745 (1984).

[20] H. Skenderović, R. Beuc, T. Ban and G. Pichler. "Blue satellite bands of KRb molecule: Intermediate long-range states". *Eur. Phys. J. D* **19**, 49–56 (2002).

[21] A. J. Ross, C. Effantin, P. Crozet and E. Boursey. "The ground state of KRb from laser-induced fluorescence". *J. Phys. B: At. Mol. Opt. Phys.* **23**, L247–L251 (1990).

[22] C. Amiot and J. Vergés. "The KRb ground electronic state potential up to 10 Å". *J. Chem. Phys.* **112**, 7068–7074 (2000).

[23] A. Pashov, O. Docenko, M. Tamanis, R. Ferber, H. Knöckel and E. Tiemann. "Coupling of the $X^1\Sigma^+$ and $a^3\Sigma^+$ states of KRb". *Phys. Rev. A* **76**, 022511 (2007).

[24] K. Alps, A. Kruzins, M. Tamanis, R. Ferber, E. A. Pazyuk and A. V. Stolyarov. "Fourier-transform spectroscopy and deperturbation analysis of the spin-orbit coupled $A^1\Sigma^+$ and $b^3\Pi$ states of KRb". *J. Chem. Phys.* **144**, 144310 (2016).

[25] N. Okada, S. Kasahara, T. Ebi, M. Baba and H. Katô. "Optical-optical double resonance polarization spectroscopy of the $B^1\Pi$ state of $^{39}K^{85}Rb$." *J.Chem.Phys.* **105**, 3458–65 (1996).

[26] S. Kasahara, C. Fujiwara, N. Okada, H. Katô and M. Baba. "Doppler-free optical-optical double resonance polarization spectroscopy of the $^{39}K^{85}Rb$ $1^1\Pi$ and $2^1\Pi$ states". *J.Chem.Phys.* **111**, 8857–66 (1996).

[27] C. Amiot, J. Vergés, C. Effantin and J. d'Incan. "The KRb $(2)^1\Pi$ electronic state". *Chemical Physics Letters* **321**, 21–24 (2000).

[28] C. Amiot, J.Vergés, J. d'Incan and C. Effantin. "The $(3)^1\Pi - (3)^1\Sigma$ system of KRb". *Chem. Phys. Lett.* **315**, 55–60 (1999).

[29] Amiot C. "The KRb $(2)^3\Sigma^+$ Electronic State," *J. Mol. Spectrosc.* **203**, 126–131 (2000).

[30] Y. Lee, C. Yun, Y. Yoon, T. Kim and B. Kim. "The 530 nm system of KRb observed in a pulsed molecular beam: New electric quadrupole transitions $(1^1\Delta - X^1\Sigma^+)$". *J. Chem. Phys.* **115**, 7413–7419 (2001).

[31] Y. Lee, Y. Yoon, B. Kim, L. Li and S. Lee. "Observation of the $3^3\Sigma^+ - X^1\Sigma^+$ transition of KRb by resonance enhanced two-photon ionization in a pulsed molecular beam: Hyperfine structures of $^{39}K^{85}Rb$ and $^{39}K^{87}Rb$ isotopomers". *J. Chem. Phys.* **120**, 6551–6556 (2004).

[32] Y. Lee, Y. Yoon, A. Muhammad, J.-T. Kim, S. Lee and B. Kim. "The 480 nm system of KRb: $1^3\Delta_1$, $4^1\Sigma^+$, and $5^1\Sigma^+$ states". *J. Phys. Chem. A* **114**, 7742–7748 (2010).

[33] Y. Lee, Y. Yoon, J. Kim, S. Lee and B. Kim. "Unravelling Complex Spectra of a Simple Molecule: REMPI Study of the 420 nm Band System of KRb". *ChemPhysChem* **12**, 2018–2023 (2011).

[34] J. T. Kim, D. Wang, E. E. Eyler, P. L. Gould and W. C. Stwalley. "Spectroscopy of $^{39}K^{85}Rb$ triplet excited states using ultracold $a^3\Sigma^+$ state molecules formed by photoassociation". *New J. Phys.* **11**, 055020 (2009).

[35] J.-T. Kim, Y. Lee, B. Kim, D. Wang, W. C. Stwalley, Ph. L. Gould and E. E. Eyler. "Spectroscopic analysis of the coupled $1^1\Pi$, $2^3\Sigma+$ $(\Omega = 0^-, 1)$, and $b^3\Pi(\Omega = 0^\pm, 1, 2)$ states of the KRb molecule using both ultracold molecules and molecular beam experiments". *Phys. Chem. Chem. Phys.* **13**, 18755–18761 (2011).

43

[36] Kim, Y. Lee, B. Kim, D. Wang, W. C. Stwalley, P. L. Gould J.-T and E.E. Eyler. "Spectroscopic prescription for optimal stimulated Raman transfer of ultracold heteronuclear molecules to the lowest rovibronic level". *Phys. Rev. A* **84**, 062511 (2011).

[37] K. Aikawa, D. Akamatsu, M. Hayashi, J. Kobayashi, M. Ueda and S. Inouye. "Predicting and verifying transition strengths from weakly bound molecules". *Phys. Rev. A* **83**, 042706 (2011).

[38] J. Banerjee, D. Rahmlow, R. Carollo, M. Bellos, E. E. Eyler, P. L. Gould and W. C. Stwalley. "Spectroscopy and applications of the $3^3\Sigma^+$ electronic state of ^{39}K^{85}Rb". *J. Chem. Phys.* **139**, 174316 (2013).

[39] D. Wang, J. T. Kim, C. Ashbaugh, E. E. Eyler, P. L. Gould and W. C. Stwalley. "Rotationally resolved depletion spectroscopy of ultracold KRb molecules". *Phys. Rev. A* **75**, 032511 (2007).

[40] P. Cavaliere, G. Ferrante and L. Lo Cascio. "Interpolated values of spectroscopic constants of asymmetric alkali molecules and molecular ions". *J. Chem. Phys.* **62**, 4753–4756 (1975).

[41] F. Jenc. "Estimation of the dissociation energy of KRb by the reduced potential energy curve (RPC) method". *J. Mol. Spectrosc.* **147**, 274–276 (1991).

[42] F. Jenc and B. A. Brandt. "Estimation of the dissociation energy and the ground state potential of KRb by the multiparameter generalized reduced potential curve (GRPC) method". *J. Mol. Spectrosc.* **154**, 226–228 (1992).

[43] O. Bludsky, M. Jurek, V. Spirko, B. Brandt and F. Jenc. "Calculation and Prediction of the Spectrum of Diatomic Molecules by the Generalized Reduced Potential Curve (GRPC) Method". *J. Mol. Spectrosc.* **169**, 555–582 (1995).

[44] William C. Stwalley. "Improved dissociation energy of the ^{39}K^{85}Rbmolecule". *J. Chem. Phys.* **122**, 084319 (2005).

[45] B. Bussery, Y. Achkara and M. Aubert-Frécon. "Long-range molecular states dissociating to the three or four lowest asymptotes for the ten heteronuclear diatomic alkali molecules". *Chem. Phys.* **116**, 319–338 (1987).

[46] S. H. Patil and K. T. Tang. "Multipolar polarizabilities and two- and three-body dispersion coefficients for alkali isoelectronic sequences". *J. Chem. Phys.* **106**, 2298–2305 (1997).

[47] M. Marinescu and H. R. Sadeghpour. "Long-range potentials for two-species alkali-metal atoms". *Phys. Rev. A* **59**, 390 (1999).

[48] A. Derevianko, J. F. Babb and A. Dalgarno. "High-precision calculations of van der Waals coefficients for heteronuclear alkali-metal dimers". *Phys. Rev. A* **63**, 052704 (2001).

[49] S. G. Porsev and A. Derevianko. "Accurate relativistic many-body calculations of van der Waals coefficients C_8 and C_{10} for alkali-metal dimers". *J. Chem. Phys.* **119**, 844–850 (2003).

[50] T. Leininger and G. Jeung. "Calculation of the weakly coupled 1 and $2\,^1\Pi$ twin states of KRb". *Phys. Rev. A* **51**, 1929 (1995).

[51] T. Leininger, H. Stoll and G. Jeung. "The 1 and $2\,^1\Pi$ twin states of KRb revisited". *J. Chem. Phys.* **106**, 2541–2543 (1997).

[52] A.Yiannopoulou, T. Leininger, A. M. Lyyra and G.-H. Jeung. "Theoretically calculated rovibronic transition spectra of KRb". *Int. J. Quantum Chem.* **57**, 575 (1996).

[53] S. Rousseau, A.R. Allouche and M. Aubert-Frécon. "Theoretical Study of the Electronic Structure of the KRb Molecule". *J. Mol. Spectrosc.* **203**, 235–243 (2000).

[54] S. Park, Y. Choi, Y. Lee and G. Jeung. "Ab initio calculations of the electronic states of KRb". *Chem. Phys.* **257**, 135–145 (2000).

[55] S. Kotochigova, P. S. Julienne and E. Tiesinga. "Ab initio calculation of the KRb dipole moments". *Phys. Rev. A* **68**, 022501 (2003).

[56] W. T. Zemke, R. Côté and W. C. Stwalley. "Analysis of the $a^3\Sigma^+$ state of KRb". *Phys. Rev. A* **71**, 062706 (2005).

[57] K. Chen, C. Yang, M. Wang, X. Ma and W. Liu. "Analytical potential energy functions and spectroscopic properties for the ground and low-lying excited states of KRb". *Spectrochim. Acta A* **99**, 57–61 (2012).

[58] P. Lobacz, P. Jasik and J. E. Sienkiewicz. "Theoretical study of highly-excited states of KRb molecule". *Cent. Eur. J. Phys.* **11**, 1107–1114 (2013).

[59] D. A. Fedorov, A. Derevianko and S. A. Varganov. "Accurate potential energy, dipole moment curves, and lifetimes of vibrational states of heteronuclear alkali dimers". *J. Chem. Phys.* **140**, 184315 (2014).

[60] M. B. Shundalau, G. A. Pitsevich, A. E. Malevich, A.V. Hlinisty, A. A. Minko, R. Ferber and M. Tamanis. "Ab initio multi-reference perturbation theory calculations of the ground and low-lying electronic states of the KRb molecule". *Comp. Theor. Chem.* **11**, 35–42 (2016).

[61] S. V. Kozlov, E. A. Pazyuk and A. V. Stolyarov. "Twofold diabatization of the KRb $(1\text{–}2)^1\Pi$ complex in the framework of ab initio and deperturbation approaches". *Phys. Rev. A* **94**, 042510 (2016).

[62] S. V. Kozlov, E. A. Pazyuk and A. V. Stolyarov. "A Reduced Method of Coupled Vibrational Channels: Analysis of Regular Perturbations in the $c^3\Sigma^+_\Omega$-State of a KRb Molecule". *Opt. Spectrosc.* **125**, 464–469 (2018).

[63] P. Jasik, P. Lobacz and J. E. Sienkiewicz. "Potential energy curves, transition and permanent dipole moments of KRb". *Atomic Data and Nuclear Data Tables* **149**, 101558 (2023).

[64] R. de L. Kronig. *Band Spectra and Molecular Structure*. Cambridge University Press, 1930.

[65] J. Brown and A. Carrington. *Rotational Spectroscopy of Diatomic Molecules*. Cambridge University Press, 2003.

[66] R. Zare. *Angular Momentum: Understanding Spatial Aspects in Chemistry and Physics*. Wiley-Interscience, 1991.

[67] M. Mizushima. *The Theory of Rotating Diatomic Molecules*. John Wiley & Sons, 1975.

[68] C. R. Vidal and J. Cooper. "Heat-Pipe Oven: A New, Well-Defined Metal Vapor Device for Spectroscopic Measurements". *J. Appl. Phys.* **40**, 3370–3374 (1969).

[69] C. Vidal and M. Hessel. "Heat-Pipe Oven for Homogeneous Mixtures of Saturated and Unsaturated Vapors; Application to NaLi". *Journal of Applied Physics* **43**, 2776–2780 (1972).

[70] V. Bednarska, I. Jackowska, W. Jastrzebski and P. Kowalczyk. "A three-section heat-pipe oven for heteronuclear alkali molecules". *Measurement Science and Technology* **7**, 1291 (1996).

[71] A. Kantrowitz and J. Grey. "A High Intensity Source for the Molecular Beam. Part I. Theoretical". *Rev. Sci. Instrum.* **22**, 328–332 (1951).

[72] G. B. Kistiakowsky and W. P. Slichter. "A High Intensity Source for the Molecular Beam. Part II. Experimental". *Rev. Sci. Instrum.* **22**, 333–337 (1951).

[73] M. P. Sinha, A. Schultz and R. N. Zare. "Internal state distribution of alkali dimers in supersonic nozzle beams". *J. Chem. Phys.* **58**, 549–556 (1973).

[74] E. J. Breford, F. Engelke, G. Ennen and Karl H. Meiwes. "Crossed laser and molecular beam studies of mixed alkali dimer: preparation, perturbation and predissociation". *Faraday Discuss. Chem. Soc.* **71**, 233–252 (1981).

[75] K. Ishikawa, T. Kumauchi, M. Baba and H. Katô. "Hyperfine structure of the NaK $c^3\Sigma^+$ state and the effects of perturbation". *J. Chem. Phys.* **96**, 6423–6432 (1992).

[76] K. Matsubara, Y. Wang, K. Ishikawa, M. Baba, A. McCaffery and H. Katô. "Hyperfine structures of the triplet states of ^{23}Na^{85}Rb". *J. Chem. Phys.* **99**, 5036–5044 (1993).

[77] R. W. Boyd and J. G. Dodd. "Analysis of the pressure, density, and velocity distributions in a spectroscopic heat-pipe oven and the resulting limitations on device performance". *J.Appl.Phys.* **51**, 6058 (1980).

[78] Wolfgang Demtröder. *Laser Spectroscopy: Experimental Techniques.* **2**. Springer Verlag, 2008.

[79] *The Iodine molecule atlas.* URL: https://www.iqo.uni-hannover.de/de/arbeitsgruppen/molecular-quantum-gases/research-projects/secondary-frequency-standard/.

[80] Kiyoshi Ishikawa. "Hyperfine structure of the NaK $a^3\Sigma^+$ state: Interaction of an electron spin with the sodium and potassium nuclear spins". *J. Chem. Phys.* **98**, 1916–1924 (1993).

[81] Y. Wang, M. Kajitani, S. Kasahara, M. Baba, K. Ishikawa and H. Katô. "High resolution laser spectroscopy of the $B^1\Pi-X^1\Sigma^+$ transition of ^{23}Na^{85}Rb". *J. Chem. Phys.* **95**, 6229–6237 (1991).

[82] J. Heinze, U. Schühle, F. Engelke and C. D. Caldwell. "Doppler-free polarization spectroscopy of the $B^1\Pi_u - X^1\Sigma_g^+$ band system of K$_2$". *J. Chem. Phys.* **87**, 45–53 (1987).

[83] V. Stoyanov and A. Pashov. "Investigation on the fine and hyperfine structure of the $c^3\Sigma^+$ state in KRb". *Journal of Quantitative Spectroscopy and Radiative Transfer* **316**, 108908 (2024).

[84] W. H. Press, S. A. Teukolsky, W. T. Vetterling and B. P. Flannery. *Numerical Recipes: The Art of Scientific Computing.* Cambridge University Press, 2007.

[85] T. Prohaska et. al. "Standard atomic weights of the elements 2021 (IUPAC Technical Report)". *Pure Appl. Chem.* **94(5)**, 573–600 (2022).

[86] Hajime Katô. "Energy Levels and Line Intensities of Diatomic Molecules. Application to Alkali Metal Molecules". *Chem. Soc. Jpn.* **99**, 3203–3234 (1993).

[87] E. Arimondo, M. Inguscio and P. Violino. "Experimental determinations of the hyperfine structure in the alkali atoms". *Rev. Mod. Phys.* **49**, 31 (1977).

[88] P. Kowalczyk. "High resolution laser spectroscopy of the $c^3\Sigma^+\leftarrow X^1\Sigma^+$ and $b^3\Pi\leftarrow X^1\Sigma^+$ forbidden transitions in NaK". *J. Chem. Phys.* **91**, 2779–2789 (1989).